Mon. Not. R. Astron. Soc. **351,** 997–1014 (2004) doi:10.1111/j.1365-2966.2004.07842.x

VLT spectropolarimetry of two powerful radio galaxies at $z \sim 1.4$: ultraviolet continuum, emission-line properties and the nature of high-redshift dust

C. Solórzano-Iñarrea,[1⋆] P. N. Best,[1] H. J. A. Röttgering[2] and A. Cimatti[3]

[1] *Institute for Astronomy, University of Edinburgh, Royal Observatory, Edinburgh EH9 3HJ*
[2] *Sterrewacht Leiden, Postbus 9513, 2300 RA Leiden, the Netherlands*
[3] *Istituto Nazionale di Astrofisica, Osservatorio Astrofisico di Arcetri, Largo E. Fermi 5, 50125 Firenze, Italy*

Accepted 2004 March 14. Received 2004 February 24; in original form 2003 December 23

ABSTRACT

Deep spectropolarimetric observations, obtained with the Very Large Telescope, are presented for two powerful radio galaxies, 0850–206 ($z = 1.3373$) and 1303+091 ($z = 1.4093$). These observations cover the rest-frame wavelength range ∼1450–3750 Å. New radio observations and continuum images of the same sources are also presented. These galaxies are the first two observed from a complete sample of nine radio sources with redshifts in the range $1.3 \leqslant z \leqslant 1.5$ (selected from the equatorial sample of powerful radio sources of Best, Röttgering & Lehnert), as part of a project aimed to investigate the multicomponent nature of the ultraviolet (UV) continuum in radio galaxies and, in particular, any variations of the continuum properties with the radio source age.

The larger radio source of the two, 0850–206, presents a high continuum fractional polarization, averaging 17 per cent across the observed wavelength range and reaching 24 per cent at rest-frame wavelengths of $\lesssim$2000 Å. The smaller radio source, 1303+091, shows a lower continuum polarization, averaging 8 per cent and rising to 11 per cent for rest-frame wavelengths $\gtrsim$3000 Å. For both galaxies, the position angle of the electric vector is generally constant with wavelength and within ∼15° of perpendicular to the radio axis. Both their total flux spectra and polarized flux spectra reveal the 2200-Å dust feature, and comparison with dust scattering models suggests that the composition of the dust in these galaxies is similar to that of Galactic dust. In 0850–206, scattered quasar radiation dominates the UV continuum emission, with the nebular continuum accounting for no more than ∼22 per cent and no requirement for any additional emission component such as emission from young stars. In contrast, in 1303+091, unpolarized radiation could be a major constituent of the UV continuum emission, with starlight accounting for up to ∼50 per cent and the nebular continuum accounting for ∼11 per cent.

The emission-line properties of the galaxies are also studied from their total intensity spectra. Comparison of the measured emission-line ratios with both shock- and photoionization models shows that the nuclear and extended gas in these galaxies is mainly photoionized by the central active nucleus.

Key words: polarization – scattering – galaxies: active – galaxies: evolution – galaxies: ISM – radio continuum: galaxies.

1 INTRODUCTION

The galaxies associated with powerful extragalactic radio sources are uniquely important for understanding the physics of active galactic nuclei (AGN) and for studying the relationship between radio source activity and the properties of the host galaxy and its environment. Powerful distant radio galaxies are thought to be the progenitors of present-day, giant ellipticals (e.g. Best, Longair & Röttgering 1998; McLure & Dunlop 2000). However, compared with normal elliptical galaxies, powerful radio galaxies at $z \gtrsim 0.6$

⋆E-mail: csi@roe.ac.uk

show enhanced optical/ultraviolet (UV) continuum and line emission, which is generally elongated and aligned along the radio axis (e.g. McCarthy et al. 1987).

The emission-line structures usually extend large distances from the nucleus (5 $\sim$ 100 kpc; e.g. Tadhunter 1986; Baum et al. 1988); the properties of these extended emission-line regions (EELR) can be greatly influenced by shocks resulting from interactions between the radio source structures and the interstellar/intergalactic medium (ISM/IGM) (e.g. Clark et al. 1998; Solórzano-Iñarrea, Tadhunter & Axon 2001; Solórzano-Iñarrea & Tadhunter 2003). Interestingly, the emission-line properties of a sample of $z \sim 1$ radio galaxies have been found to evolve strongly as the radio source passes through the host galaxy (Best, Röttgering & Longair 2000a): large radio sources ($\gtrsim$150 kpc) show quiescent 'rotation-dominated' velocity profiles and ionization states in agreement with AGN-illumination, while smaller radio sources present highly distorted kinematic profiles and overall ionizations consistent with being shock-dominated.

As for the optical/UV continuum excess observed in radio galaxies, several different mechanisms are known to contribute to it (e.g. Tadhunter et al. 2002), but the relative extent of their contributions remains uncertain. A popular early interpretation for this UV excess was recent star formation, induced by the passage of the radio jet through the ISM of the host galaxy or by merger events linked to the radio source triggering (e.g. Rees 1989). Jet-induced star formation has been shown to be feasible in numerical simulations (e.g. Mellema, Kurk & Röttgering 2002). Also, stellar absorption features characteristic of OB stars have been observed in the radio galaxy 4C41.17 at $z = 3.8$ (Dey et al. 1997).

The detection of polarized continuum and polarized broad permitted emission lines in some radio galaxies (e.g. Antonucci & Miller 1985; di Serego Alighieri et al. 1989; Cimatti et al. 1993) suggested that light emitted anisotropically by a hidden quasar nucleus and scattered towards us by dust or electrons in the ISM of the radio galaxy (Tadhunter, Fosbury & di Serego Alighieri 1988; Fabian 1989) also makes an important contribution to the UV light. This is favoured by orientation-based unified schemes for radio sources (Barthel 1989), according to which radio galaxies and quasars are drawn from the same parent population but viewed from different angles to the line of sight, with the AGN in radio galaxies obscured by a surrounding dusty torus. Spectropolarimetric studies of a small number of radio galaxies at $z \sim 1$ have shown that the polarized emission is spatially extended, with the electric vector oriented perpendicular to the UV continuum emission at all wavelengths, and that, while the permitted Mg II 2800 emission line is observed to be broad in polarized light, none of the narrow lines shows significant polarization (e.g. Cimatti et al. 1996, 1997). These results clearly show that the origin of the polarization is scattered quasar light. More recent spectropolarimetric studies of a sample of radio galaxies at $z \sim 2.5$ (Vernet et al. 2001) have shed light on the nature of the scattering material. These studies show indications of a continuum upturn beyond 2200 Å in the composite spectrum of the galaxies in the sample, which is interpreted as a possible detection of the 2200-Å dust feature, indicating that the scattering medium is dust. However, caution must be taken because, due to the high redshift of their sample, those wavelengths are redshifted into a region of strong sky lines.

Together with the young stellar and scattered AGN components, other processes known to contribute to the UV continuum excess in some sources are nebular continuum emitted by the extended emission-line gas (Dickson et al. 1995) and direct AGN light (Shaw et al. 1995).

As with the emission-line gas, some properties of the continuum emission in radio galaxies are observed to vary with radio source size: smaller sources show strings of bright knots aligned along the radio axis, and larger sources present more compact nebulae with fewer bright components (Best, Longair & Röttgering 1996). Do the contributions of the different components to the UV excess also evolve over the radio source lifetime? For instance, a large variation is seen in the strengths, and to a lesser extent colours, of the polarized emission in radio galaxies. Is this linked to the radio source size? Such questions cannot be answered by existing spectropolarimetric data, because targets were generally selected on the basis of previously detected polarization in imaging observations, an interesting UV morphology or an ultrasteep radio spectrum, making the samples studied biased or incomplete.

To remedy this and address many of the issues raised above, such as the nature of the scatterers at high redshift and the variation with radio source size of the different contributions to the UV excess, we have begun a programme to make deep spectropolarimetric observations of a *complete* sample of nine radio galaxies with redshifts in the range $1.3 \leqslant z \leqslant 1.5$ and a wide range in radio sizes. In this paper we present the observations of the first two galaxies from the sample.

The paper is organized as follows. In Section 2, the selection criteria of our sample are described. Section 3 contains the details of the observations, data reduction and analysis. The results are presented in Sections 4 and 5. Discussion of the results follows in Section 6. Summary and conclusions are provided in Section 7. Throughout this paper values of the cosmological parameters of $H_0 = 65$ km s^{-1} Mpc^{-1}, $\Omega_M = 0.3$ and $\Omega_\Lambda = 0.7$ are assumed.

2 SAMPLE SELECTION

The sources of our full sample comprise all radio galaxies from the equatorial sample of powerful radio sources of Best, Röttgering & Lehnert (1999b),[1] with redshifts in the range $1.3 \leqslant z \leqslant 1.5$. The redshift range was chosen to be low enough to allow good signal-to-noise (S/N) ratio, but also sufficiently high to ensure that the rest-frame wavelengths studied ($\sim$1400–3800 Å) allowed to search for features in the dust scattering cross-section around 2200 Å, and stellar absorption lines, such as Si III 1417, S V1502 and N IV1720. Furthermore, this wavelength range covers the He II 1640 emission line, which can be used as a replacement for the Balmer lines to derive the amount of nebular continuum emission. Our sample also includes sources with a wide range of radio sizes, from $\sim$10 to 400 kpc, in order to investigate variations of the emission-line and continuum properties with the radio source age.

The results obtained from the first two sources observed from our sample are presented in this paper. Properties of these two sources are listed in Table 1.

3 OBSERVATIONS, DATA REDUCTION AND ANALYSIS

3.1 Very Large Telescope observations

Optical imaging and spectropolarimetric observations were carried out on the 8.2-m ESO Very Large Telescope (VLT) Antu (UT1) at

[1] Following the additional identifications and redshifts of Best, Röttgering & Lehnert (2000b) and Best et al. (2003), this radio source sample is now 100 per cent spectroscopically complete.

Table 1. Properties of the two radio galaxies from our sample presented in this paper. The redshift of each source, derived from the data presented in this paper, is given in column 2. Column 3 gives the projected extent of the radio source along the radio axis (Best et al. 1999b). The position angle of the radio axis for each source (Best et al. 1999b) is listed in column 4. The last column gives the colour excess E_{B-V} for each source taken from NASA/IPAC Extragalactic Data base (NED).

Source	z	$D_{\rm rad}$ (kpc)	$\rm PA_{rad}$ (deg)	E_{B-V} (mag)
0850−206	1.3373 ± 0.0018	118	29	0.242
1303+091	1.4093 ± 0.0012	73	131	0.030

Table 2. Log of the VLT optical imaging observations. Photometric magnitudes, measured through 2- and 4-arcsec diameter apertures, are also given.

Source	Filter	$\lambda_{\rm cen}$ (Å)	$t_{\rm exp}$ (s)	Magnitude 2 arcsec	Magnitude 4 arcsec	Airm.
0850–206	V_BESS	5540	300	22.98	22.73	1.024
0850–206	I_BESS	7680	300	21.79	21.39	1.018
1303+091	I_BESS	7680	300	21.83	21.40	1.724

Paranal (Chile) on the nights of 2000 January 31 and February 1. The imaging spectrograph FORS1 was used in both direct imaging (IMG) and multi-object spectropolarimetry (PMOS) modes together with the Tek 2048 × 2048 CCD, which provides a spatial scale of 0.2 arcsec pixel^{-1}. Observations were made under good seeing conditions, averaging 0.5 and 0.7 arcsec for the two nights, respectively. The first night was clear, but part of the second night was non-photometric. Details of the observations are presented in Tables 2 and 3.

3.1.1 Optical imaging

Imaging observations were made through the broad-band filters V_BESS+35 for 0850–206, and I_BESS+37 for both 0850–206 and 1303+091.

The reduction of the imaging data was performed using standard tasks within the IRAF software package, following the usual steps. The bias was first subtracted and then the images were flat-fielded using sky flats. Photometric calibration was achieved by using observations of the photometric standard stars PG 0231+051 and PG 1323–086 taken during the nights. The Johnson photometric magnitudes, measured through 2- and 4-arcsec diameter apertures, are given in Table 2.

3.1.2 Optical spectropolarimetry

The grism GRIS_300V was used for the spectropolarimetric observations, providing a spectral dispersion of approximately 2.6 Å pixel^{-1}. For the source 0850–206 a 1.4-arcsec slit was oriented along the axis defined by the position of optical objects, which is misaligned by approximately 35° with the radio axis (see Fig. 1, left-hand panel). In the case of 1303+091, a 1-arcsec slit was oriented parallel to the radio axis (see Fig. 6, left-hand panel). Note that the imaging spectrograph FORS has a compensator that corrects for atmospheric dispersion. Four sets of observations were made for each source (two sets on each night), each set consisting of four exposures with the half-wave plate position angle rotated to 0°, 22.°5, 45° and 67.°5, consecutively. 0850–206 was observed in three sets of four 1350-s exposures and one set of four 900-s exposures, with a total integration time of 5.5 h. 1303+091 was observed in two sets of four 1350 s, one set of four 900 s and one set of three 1150 s (the 67.°5 exposure was lost due to instrument problems), making a total integration time of nearly 5 h. The last two sets of 1303+091 were carried out in non-photometric conditions.

The reduction of the spectropolarimetric data was performed using IRAF in the following way. The frames were first bias-subtracted and then flat-fielded using lamp flats taken through the same optics used in the source and star frames. After removing cosmic ray events, the different exposures for the same half-wave plate positions were combined for each source. In the case of 1303+091, appropriate weights and scales were applied to account for the non-photometric conditions in which this source was observed during the second night. One-dimensional spectra, with identical aperture widths for the ordinary (o) and extraordinary (e) rays for each of the four half-wave plate orientations, were then extracted. The wavelength calibration was performed using He, HgCd and Ar arc lamps. After that, o- and e-rays were resampled to the same linear spectral dispersion, in order to calculate the polarization over identical spectral bins. The data were then binned, and all eight one-dimensional spectra were combined to determine the Stokes parameters I, Q and U for each galaxy, using the procedures described in Vernet (2001; see also Vernet et al. 2001), which are based on the method outlined in Cohen et al. (1995). Observations of polarized (HD245310 and HD111579) and unpolarized (HD64299 and HD94851) standard stars (Turnshek et al. 1990; Schmidt, Elston & Lupie 1992) were taken in order to check and calibrate the instrumental polarization and the position angle zero-point offset. Flux calibration was provided by observations of the spectrophotometric standard stars Feige 24 and G163–50. The atmospheric extinction correction was achieved by using the extinction curve of La Silla Observatory, since no suitable data for Paranal are available.

No second-order filter was used in these observations, but instead the polarized standard star HD245310 was observed both with and without the GG435 filter, which blocks the light below 4200 Å, to estimate the effects of any second-order blue light. Residual second-order light, which only affects the spectral region with $\lambda \gtrsim 7000$ Å, was found to be very low. In addition, the continuum polarization of the star HD245310 was derived for both sets of observations (with and without filter), and it was found that it did not vary in any significant way. Thus, any contamination by second-order blue light does not affect the conclusions of this paper.

For the analysis of the total flux spectra, the two-dimensional frames of the o- and e-rays were first corrected for any distortion along the spectral direction, using the Starlink FIGARO package, and

Table 3. Log of the VLT optical spectropolarimetric observations. The spectral resolution given is that of the observed frame.

Source	$t_{\rm exp}$ (s)	Slit PA (deg)	Grism	λ range (Å)	Pixel scale (arcsec Å^{-1})	Resolution (Å)	Slit width (arcsec)	Airmass
0850–206	19 800	175	GRIS_300V	3460–8792	0.2/2.607	14.66 ± 0.10	1.4	1.19
1303+091	17 850	131	GRIS_300V	3281–8583	0.2/2.593	11.27 ± 0.07	1.0	1.36

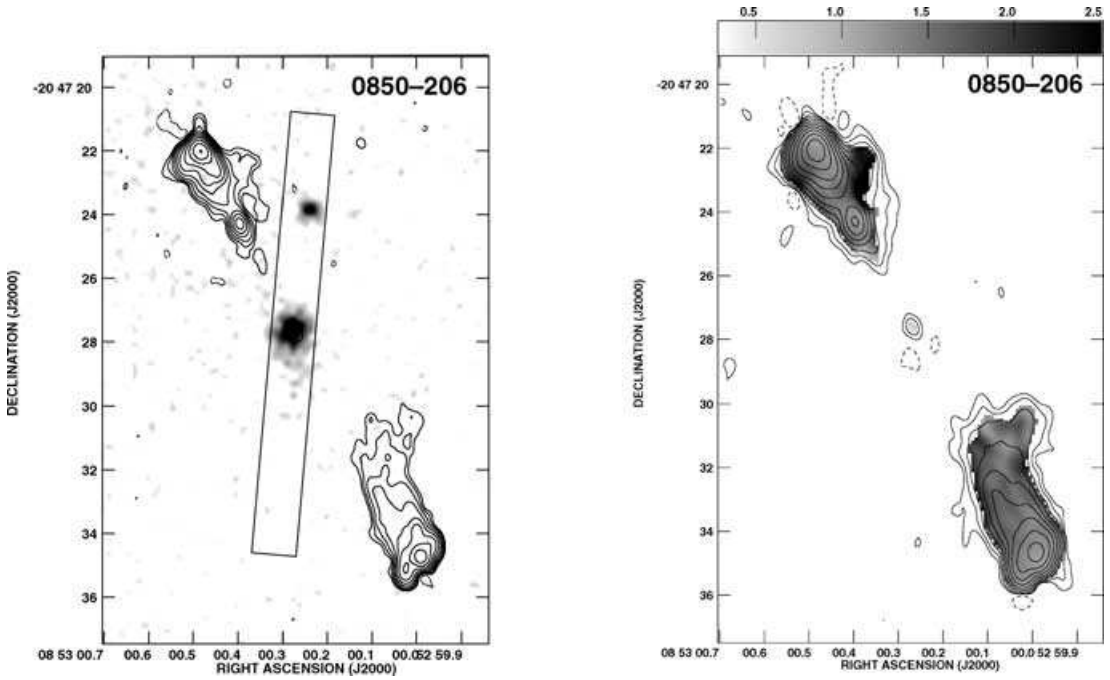

Figure 1. Left: *V*-band image of 0850–206 overlaid with contours of the radio emission at 8.5 GHz. The values of the radio contours are 1×10^{-4} Jy beam^{-1} $\times$ (-1, 1, 2, 4, 8, 16, 32, 64, 128, 256, 512). The position of the slit is also indicated on the left plot (the length of the slit is arbitrary). Right: radio spectral index, α (grey-scale, defined as $S_\nu \propto \nu^{-\alpha}$), between 8.5 and 4.7 GHz for 0850–206. Overlaid are contours of radio emission at 4.7 GHz, with contour levels of 1.7×10^{-4} Jy beam^{-1} $\times$ (-1, 1, 2, 4, 8, 16, 32, 64, 128, 256, 512). The bright radio knot at RA $= 08^{\rm h}53^{\rm m}00\overset{\rm s}{.}27$ Dec. $= -20^\circ47'27\overset{''}{.}6$ has the flattest spectral index, $\alpha \approx 0.4$ which is typical of radio cores at these redshifts (e.g. Athreya et al. 1997).

then summed. After that, one-dimensional spectra were extracted, and then analysed using the Starlink DIPSO spectral analysis package. Emission-line fluxes, velocity shifts and linewidths (FWHM) were obtained by Gaussian fitting of the emission-line profiles. The measured linewidths were corrected for the spectral resolution of the instrument via Gaussian deconvolution. The instrumental resolution was measured from night-sky lines and arc lines, and is listed in Table 3.

The total intensity spectra, emission-line fluxes and ratios have been corrected for Galactic reddening using the extinction curve from Seaton (1979) and values of colour excess E_{B-V} from the NASA/IPAC Extragalactic Data Base (NED; see Table 1).

Table 4. Log of the VLA radio observations.

Source	Freq. (MHz)	Array (Config.)	Obs. date (d/m/y)	$t_{\rm exp}$ (min)
0850–206	8460	A	09/12/2000	56
		B	20/05/2001	16
0850–206	4710	A	09/12/2000	38
		B	20/05/2001	15
1303+091	8460	A	11/12/2001	55
		B	20/05/2001	16
1303+091	4710	A	11/12/2001	33
		B	20/05/2001	15

3.2 Radio observations

New radio observations of all nine sources in the spectropolarimetric sample were carried out using the Very Large Array radio interferometer. Each source was observed using the A-array configuration at both 8.5- and 4.7-GHz frequencies, mapping both the total intensity and polarization properties. Sources larger than 10 arcsec in angular extent were additionally mapped using the B-array configuration in order to provide sensitivity to the extended structures. Full details of all of these observations will be provided elsewhere (Best et al., in preparation). Here, only the total intensity data for 0850–206 and 1303+091 are considered, to compare the radio properties with the spectropolarimetric and imaging data and to use the radio spectral index information to locate the radio cores.

Details of the observations of these two sources are provided in Table 4. Data reduction for both sources followed the standard procedures of CLEANing and self-calibration within the AIPS package (e.g. see Best et al. 1999a). 8.5-GHz total intensity maps were made at full angular resolution ($\approx$0.3 arcsec), with rms noise levels of 22 μJy. Maps were also made at lower angular resolutions matching those of the 4.7-GHz data (0.45 arcsec for 1303+091; 0.67 arcsec by 0.45 arcsec for 0850–206), by weighting down the outer regions of the UV-plane. These matched-resolution 8.5- and 4.7-GHz maps were aligned and combined to produce a radio spectral index map of each source.

3.3 Registration of the radio and optical images

The optical and radio maps of the two galaxies were aligned by assuming that the continuum centroid of the optical emission was coincident with the location of the radio core, adopted to be the radio knot with the flattest spectral index (see Fig 1, right-hand panel and Fig. 6, right-hand panel). As a check, astrometry was also performed on the optical images by using several unsaturated stars present in the observed fields and in the APM (Maddox et al. 1990) and US Naval Observatory catalogues.

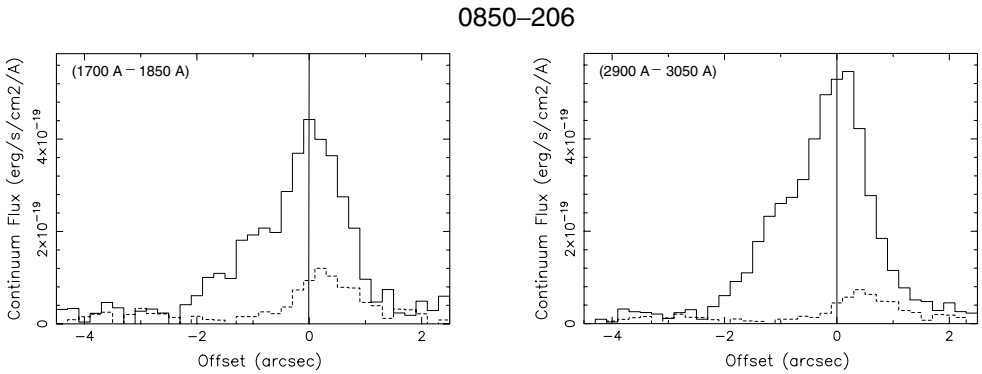

Figure 2. Spatial profiles of the line-free continuum emission (solid line) along the slit for 0850–206, between 1700–1850-Å rest-frame (left-hand panel) and between 2900–3050-Å rest-frame (right-hand panel). The dashed line shows the nebular continuum profile for the same wavelength ranges (see Section 6.1). South is to the left.

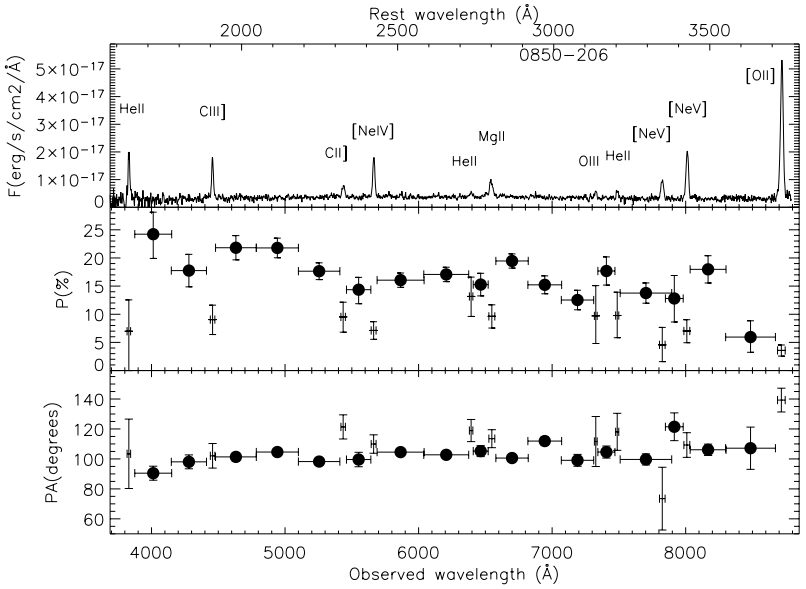

Figure 3. Spectral and polarization properties of the radio galaxy 0850–206. From top to bottom: the total flux spectrum, the observed fractional polarization and the position angle of the electric vector. Filled circles and crosses indicate, respectively, continuum bins and emission line bins with their underlying continuum.

4 0850–206

4.1 The continuum emission

Fig. 1 (left-hand panel) presents the VLT image of the radio galaxy 0850–206 in the *V* band, overlaid with contours of the radio emission at 8.5 GHz. The position of the slit for the spectropolarimetric observations is also shown in the figure. The central wavelength of the V-filter in the rest frame of the galaxy was 2370 Å, with a bandwidth of 440 Å (rest-frame).

Fig. 2 shows the spatial profile of the line-free continuum emission (solid line) along the slit for 0850–206, for the rest-frame wavelength ranges 1700–1850 (left-hand panel) and 2900–3050 Å (right-hand panel). It appears that the total continuum emission in the UV end is slightly weaker than that at longer wavelengths.

4.1.1 Polarization of the continuum emission

The spectropolarimetric results of 0850–206 are presented in Fig. 3. From top to bottom the following are plotted: the total flux spectrum, the percentage polarization and the position angle of the electric vector. A 2 arcsec-wide (∼18-kpc) aperture centred on the continuum centroid was used for the extraction of 1D spectra for the o- and e-rays.

The continuum fractional polarization of this source is observed to increase gradually towards shorter wavelengths, with an average value of 17 per cent across the observed wavelength range of the spectrum. The highest polarization is measured in the bin longward of He II 1640, with a value of $24.2^{+3.9}_{-4.3}$ per cent. Note that the polarization measured in the bin shortward of [O II] 3727, with a value of 6 per cent, may be affected by noise due to the strong sky lines in that spectral region.

The position angle of the electric vector is generally constant with wavelength, with an average value of 103°, which is within ∼15° perpendicular to the radio axis ($PA_{rad} \sim 29°$, defined by the position of the two most distant radio hotspots). For shorter rest-frame wavelengths than 1900 Å, the position angle seems to decrease slightly down to a value of ∼90°. Previous studies of high-z radio galaxies show a better perpendicularity between the electric vector and the UV continuum axis than with the radio axis

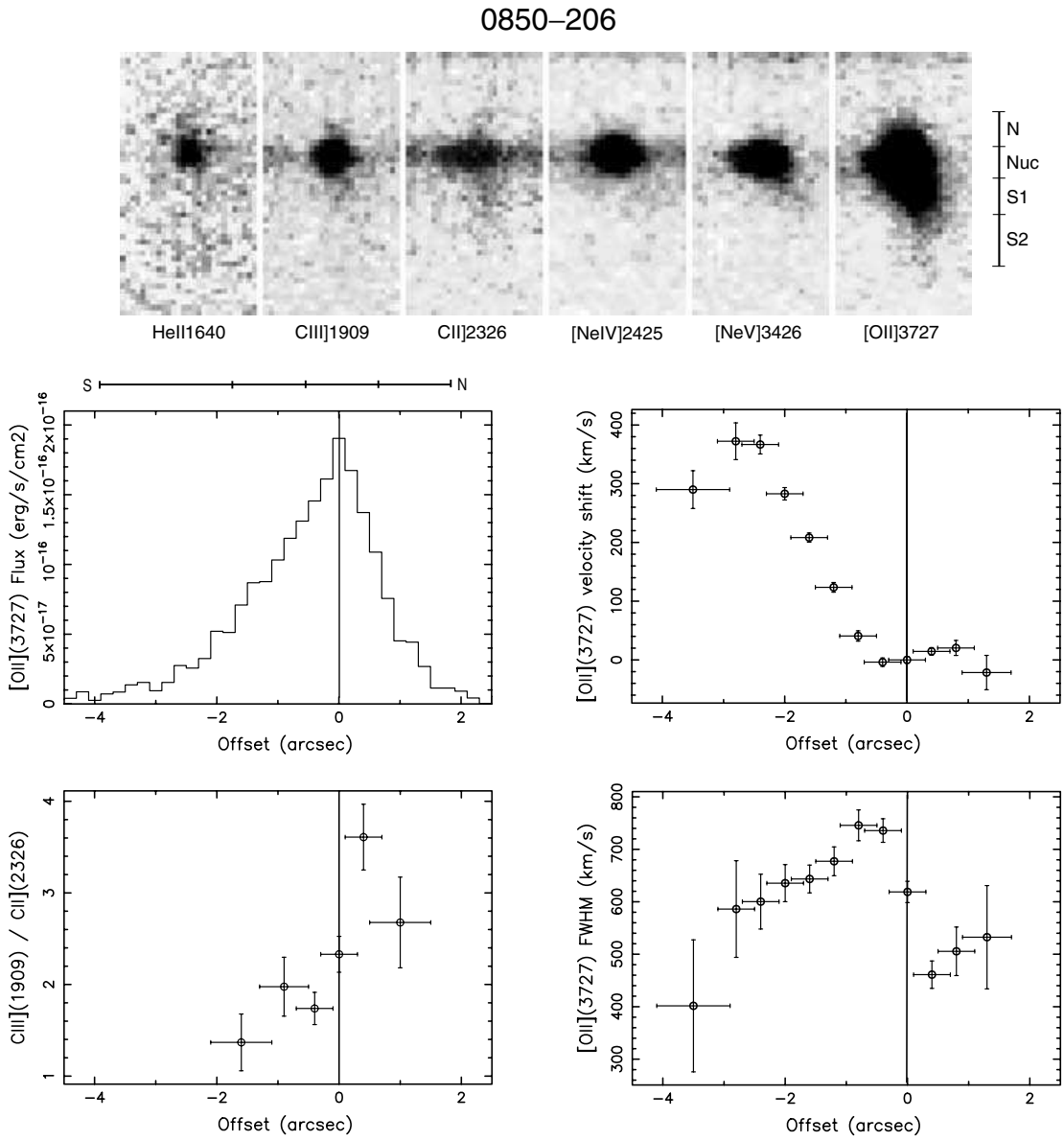

Figure 4. Top panel: 2D spectra of the main emission lines for 0850–206. Each spectrum covers 9.6 arcsec along the slit, and 30 Å (rest-frame) in the spectral direction. The regions defined along the slit are indicated by the solid line at the right of the panel. Bottom panel: emission-line spatial analysis along the slit for 0850–206. Top left: variation of the [O II] 3727 flux. The spatial regions defined along the slit are indicated by a solid line at the top of the plot. Bottom left: spatial variation in the C III] 1909/C II] 2326 line ratio. Top right: spatial variation in the [O II] 3727 velocity centroids. Bottom right: spatial variation of the [O II] 3727 linewidth. South is to the left in the four plots.

(e.g. di Serego Alighieri, Cimatti & Fosbury 1993; Cimatti et al. 1993, 1994; di Serego Alighieri et al. 1996; Vernet et al. 2001). There are no rest-frame UV images of 0850–206 available to measure the UV axis with precision, but the UV image published in this paper (Fig. 1, left-hand panel), although not very deep, suggests that the UV axis is $12^\circ \pm 5^\circ$, which is perpendicular to the electric vector orientation. It should also be noted that previous studies of low-z narrow-line radio galaxies have shown that when there is a hidden nucleus and a polarization fan, the measured position angle of the electric vector can depend on the slit orientation (Cohen et al. 1999).

4.2 The line emission

4.2.1 Emission-line structure

2D spectra of some of the main emission lines observed for 0850–206 are shown in the top panel of Fig. 4. These are He II 1640, C III] 1909, C II] 2326, [Ne IV] 2425, [Ne V] 3426 and [O II] 3727. The spatial variation of the flux of the brightest emission line ([O II] in this case) along the slit was determined and it is presented in the same figure (bottom panel: top left). The spatial profile was derived by first extracting a spatial slice perpendicular to the dispersion

direction and centred on the [O II] emission line, with a spectral width of 60 Å. Then, to correct for the continuum contamination, a spatial slice extracted from a line-free region of the spectrum, adjacent to the emission line and scaled to have the same spectral width as that of the emission-line slice, was subtracted from the first one.

The detected [O II] emission extends approximately 6 arcsec (∼54 kpc) along the slit. The line emission distribution is observed to be asymmetric with respect to the nucleus, extending further to the south than to the north.

4.2.2 Emission-line kinematics

Kinematic information of the emission-line gas in 0850–206 was obtained by fitting single Gaussians to the profile of [O II] 3727, which was the emission line with the highest signal-to-noise ratio in the observed spectrum. To try to match the seeing of the observations, one-dimensional spectra with an aperture of 3 pixel (0.6 arcsec) and centred in steps of 2 pixel were extracted from the 2D total intensity spectrum of the galaxy. In the outermost regions of the galaxy the aperture width of the extracted 1D spectra was greater than 3 pixels in order to increase the S/N ratio of these regions.

The spatial variation along the slit of the velocity centroids and linewidth of the [O II] 3727 line for 0850-206 are shown in Fig. 4 (bottom panel: top right, bottom right).

The velocity shifts, which are referred to the velocity of the emission-line gas at the continuum centroid, are observed to vary smoothly along the position of the slit, with an overall velocity amplitude of $\Delta\, v \sim 450$ km s^{-1}. The velocity curve is, however, highly asymmetric with respect to the nucleus; while the emission-line gas at the north end, approximately 1 arcsec from the centre, appears to have a velocity comparable to that of the nucleus, the gas at ∼3 arcsec to the south of the nucleus is redshifted by approximately +400 km s^{-1}.

The instrumentally corrected linewidths (FWHM) of the [O II] line are found to range between ∼300 and 800 km s^{-1} along the location of the slit. The broadest emission lines, with FWHM ∼ 750 km s^{-1}, are located approximately 1 arcsec south of the nucleus. The nucleus itself presents [O II] linewidths of FWHM ∼ 620 km s^{-1}.

4.2.3 Emission-line spectra

The total intensity spectrum of 0850–206 (corresponding to an aperture of 2 arcsec centred on the nucleus) is shown in Fig. 3 (top). Also, integrated spectra of four different regions defined along the slit (nuclear region, southernmost 'S2', southern 'S1' and northern EELR) are presented in Fig. 5 (see the figure caption for details of the apertures). The emission-line fluxes normalized to the C II] 2326 flux for each region are listed in Table 5. C II] 2326 was chosen for the normalization of the line fluxes because it is a common line in the observed spectra of both 0850–206 and 1303+091, the emission of which is also detectable in the extended regions of the galaxies.

The spatial variation of the C III] 1909/C II] 2326 line ratio along the location of the slit for 0850–206 is shown in Fig. 4 (bottom panel: bottom left). The emission-line gas with the highest ionization state is found to be at ∼0.5 arcsec north of the nucleus, with a line ratio C III]/C II] ∼ 3.6. The nucleus itself presents a moderate ionization state in comparison with the rest of the regions observed. The gas showing the lowest ionization, with C III]/C II] ∼ 1.3, is located at ∼2 arcsec south of the nucleus, which coincides with a region of relatively broad emission lines (FWHM$_{[O\,II]}$ ∼ 660 km s^{-1}).

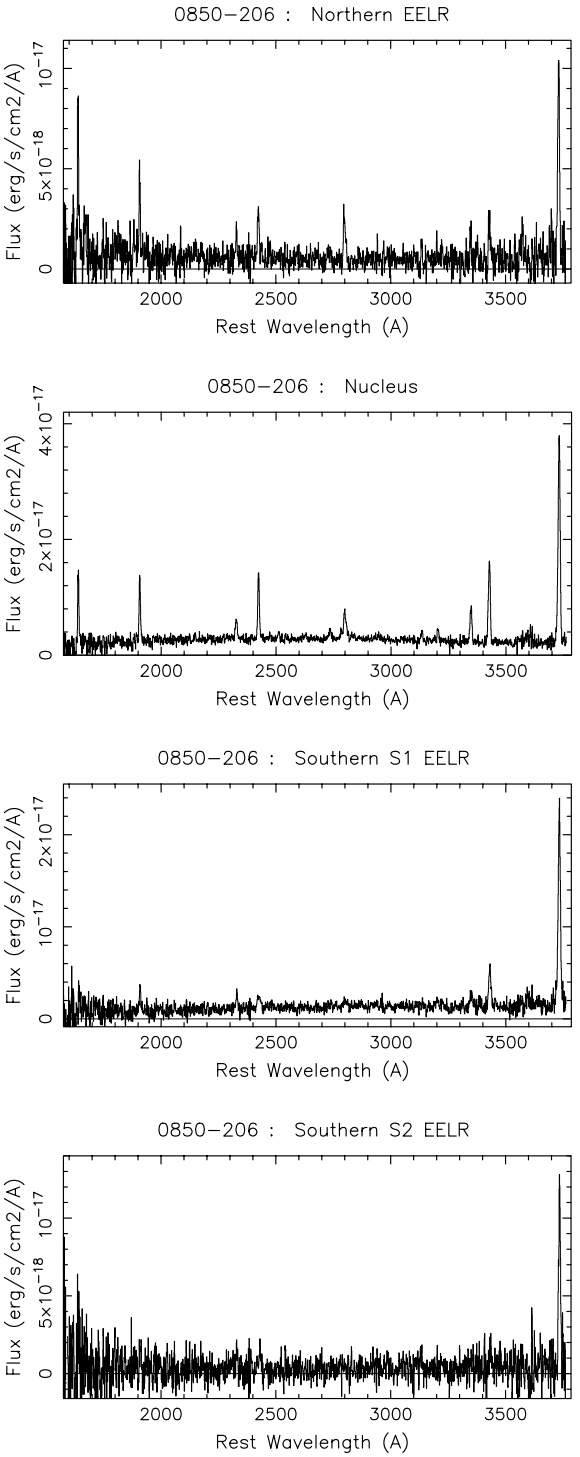

Figure 5. Integrated spectra for the different emission-line regions in 0850–206 defined along the slit: northern EELR (top; 1.2 × 1.4 arcsec^2 aperture centred at 1.1 arcsec N of the continuum centroid), nucleus (middle top; 1.2 × 1.4 arcsec^2 aperture centred at 0.1 arcsec S of the continuum centroid), southern EELR 'S1' (middle bottom; 1.2 × 1.4 arcsec^2 aperture centred at 1.3 arcsec S of the continuum centroid) and southern EELR 'S2' (bottom; 2.2 × 1.4 arcsec^2 aperture centred at 3.0 arcsec S of the continuum centroid).

4.2.4 Polarization of the emission lines

In view of the unified schemes for radio sources, it is expected that the forbidden lines are unpolarized, since they are emitted isotropically in the narrow-line region outside the obscuring torus (unless

Table 5. Emission-line integrated fluxes (corrected for Galactic reddening and normalized to the C II] 2326 flux) for the different regions in 0850–206. The details of the apertures are in the caption of Fig. 5. The quoted errors correspond to the line fitting errors.

0850–206 Line	S2 EELR (3.0 arcsec S)	S1 EELR (1.3 arcsec S)	Nucleus (0.1 arcsec S)	N EELR (0.9 arcsec N)
He II 1640	<3.28	<1.06	2.56 ± 0.21	5.22 ± 0.95
N III] 1749	–	–	0.32 ± 0.13	1.07 ± 0.46
Si III] 1882	–	–	0.18 ± 0.06	–
Si III] 1892	–	–	0.25 ± 0.06	–
C III] 1909	1.17 ± 0.43	1.37 ± 0.26	2.46 ± 0.17	2.92 ± 0.52
C II] 2326	1.00 ± 0.23	1.00 ± 0.13	1.00 ± 0.06	1.00 ± 0.16
[Ne IV] 2425	1.21 ± 0.46	1.50 ± 0.28	2.95 ± 0.18	2.19 ± 0.39
[O II] 2472	–	–	0.23 ± 0.05	–
[Mg VII] 2510	–	–	0.33 ± 0.06	–
[Mg VII] 2629	–	–	0.21 ± 0.06	–
He II 2733	–	–	0.53 ± 0.07	–
[Mg V] 2783	–	–	0.28 ± 0.05	–
Mg II 2800	–	–	1.92 ± 0.14	2.53 ± 0.44
H I 2829	–	–	0.14 ± 0.04	–
O III 3133	–	–	0.42 ± 0.06	0.64 ± 0.17
He II 3203	–	0.55 ± 0.16	0.52 ± 0.06	–
[N V] 3346	–	1.20 ± 0.24	1.80 ± 0.13	1.12 ± 0.28
[N V] 3426	<1.08	3.69 ± 0.53	4.28 ± 0.26	1.96 ± 0.41
[O II] 3727	10.88 ± 2.56	18.43 ± 2.44	11.50 ± 0.69	9.54 ± 1.55
C II] 2326 flux (10^{-17} erg s^{-1} cm^{-2})	2.42 ± 0.55	3.11 ± 0.41	7.77 ± 0.45	2.25 ± 0.35

resonantly scattered). On the other hand, the broad permitted lines, emitted in the broad-line region inside the torus, are expected to be polarized.

Fig. 3 (middle plot) shows the observed fractional polarization for continuum and emission-line bins in 0850–206, for a spatial aperture of 2 arcsec centred on the continuum centroid. It can be seen that the polarization of the emission lines (with the underlying continuum) is lower than the adjacent pure continuum bins. After subtracting the underlying continuum, the polarization of the emission lines with high enough S/N ratio was measured, obtaining the following: $P_{\rm C\,III]} = 5.1^{+3.9}_{-4.6}$, $P_{\rm [Ne\,IV]} = 3.7 \pm 2.5$, $P_{\rm [Ne\,V]} = 4.1 \pm 2.9$ and $P_{\rm [O\,II]} = 3.6 \pm 1.1$ per cent. The position angles of the electric vector for these lines range from 112° to 135°. These low polarizations (if real) could be due to transmission through magnetically aligned dust in either the radio galaxy itself or the ISM of our Galaxy: using the Galactic relation $P_{\rm ISM} < 9.0\, E_{B-V}$ (Serkowski, Mathewson & Ford 1975), the interstellar polarization due to our Galaxy could be up to ∼2.2 per cent. However, the fact that the electric vector position angles of these lines are on average almost perpendicular to the radio axis of 0850–206 ($\rm PA_{rad} \sim 29°$), suggests that the low polarization observed in these emission lines could be due to scattering or residuals of the continuum subtraction.

The continuum-subtracted polarization of the permitted Mg II line was also measured, obtaining $P_{\rm Mg\,II} = 4.6^{+4.0}_{-4.6}$ per cent and an electric vector position angle of 148° ± 24°. The errors in the polarization measurements of this line are bigger and thus no significant conclusions can be drawn concerning its polarization properties.

5 1303+091

5.1 The continuum emission

Fig. 6 (left-hand panel) shows the VLT *I*-band image of the radio galaxy 1303+091, overlaid with contours of the radio emission at 8.5 GHz. The position of the slit for the spectropolarimetric observations is indicated in the figure. The central wavelength of the I-filter in the rest frame of the galaxy was 3188 Å, with a bandwidth of 573 Å (rest-frame).

Fig. 7 shows the spatial profile of the line-free continuum emission (solid line) along the slit for 1303+091, for the rest-frame wavelength ranges 1700–1850 (left-hand panel) and 2900–3050 Å (right-hand panel). It can be seen that, unlike 0850–206, 1303+091 presents a stronger continuum emission at the UV end than at longer wavelengths.

5.1.1 Polarization of the continuum emission

Fig. 8 presents the spectropolarimetric results of 1303+091, showing from top to bottom: the total flux spectrum, the percentage polarization and the position angle of the electric vector. The aperture used for the extraction of the 1D spectra for the o- and e-rays was 2 arcsec (∼18 kpc) wide and centred on the continuum centroid.

Compared with 0850–206, 1303+091 presents an overall lower continuum fractional polarization, with an average value of 8 per cent across the observed wavelength range of the spectrum. The highest polarization is found in the bin longward of [Ne V] 3426, with a value of $11.5^{+5.6}_{-5.2}$ per cent. The polarization then, in contrast with 0850–206, is observed to decrease slightly towards shorter wavelengths. A dip is found in the bin of ∼2000 Å (rest frame) with a value of 4.8 ± 1.0 per cent. For shorter wavelengths than ∼1900 Å, the polarization is observed to increase again up to a value of $7.5^{+2.4}_{-2.5}$ per cent.

The position angle of the electric vector is fairly constant with wavelength, with an average value of 25°, which is within ∼15° perpendicular to the radio axis, defined by the position of the two most distant radio hotspots ($\rm PA_{rad} \sim 131°$), and within 7° perpendicular to the axis defined by the radio core and the south-eastern inner radio knot ($\rm PA_{knot} \sim 122°$). For longer rest frame wavelengths than ∼3300 Å, the position angle of the electric vector has values of 64° ± 10° and −5 ± 14° for the two separate bins considered; however,

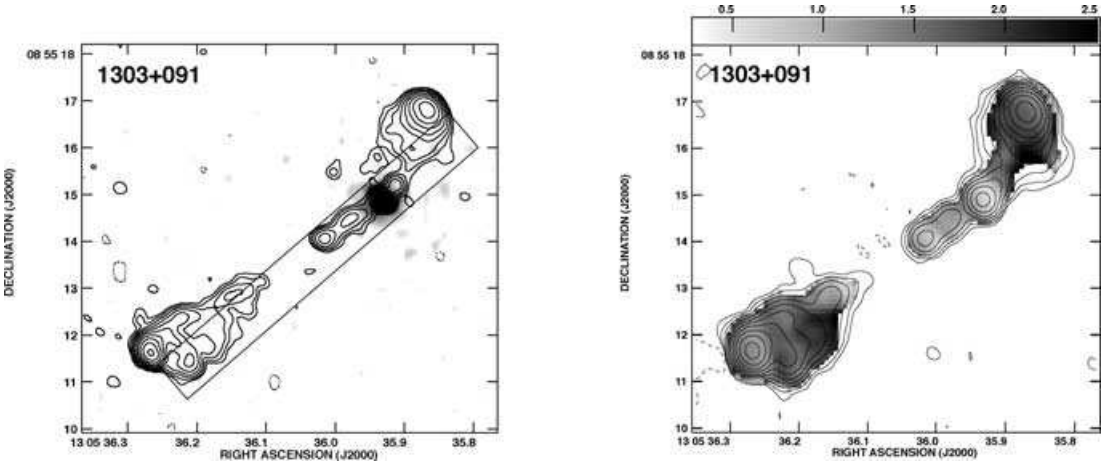

Figure 6. Left: *I*-band image of 1303+091 overlaid with contours of the radio emission at 8.5 GHz. The values of the radio contours are 7×10^{-5} Jy beam^{-1} $\times$ (-1, 1, 2, 4, 8, 16, 32, 64, 128, 256, 512). The position of the slit is also indicated (the length of the slit is arbitrary). Right: radio spectral index, α (grey-scale, defined as $S_\nu \propto \nu^{-\alpha}$), between 8.5 and 4.7 GHz for 1303+091. Overlaid are contours of radio emission at 4.7 GHz, with contour levels of 1.5×10^{-4} Jy beam^{-1} $\times$ (-1, 1, 2, 4, 8, 16, 32, 64, 128, 256, 512). The bright radio knot at RA = $13^{\rm h}05^{\rm m}35\overset{\rm s}{.}93$ Dec. = $+08^\circ55'14\overset{''}{.}9$ has the flattest spectral index, $\alpha \approx 0.5$ which is typical of radio cores at these redshifts (e.g. Athreya et al. 1997).

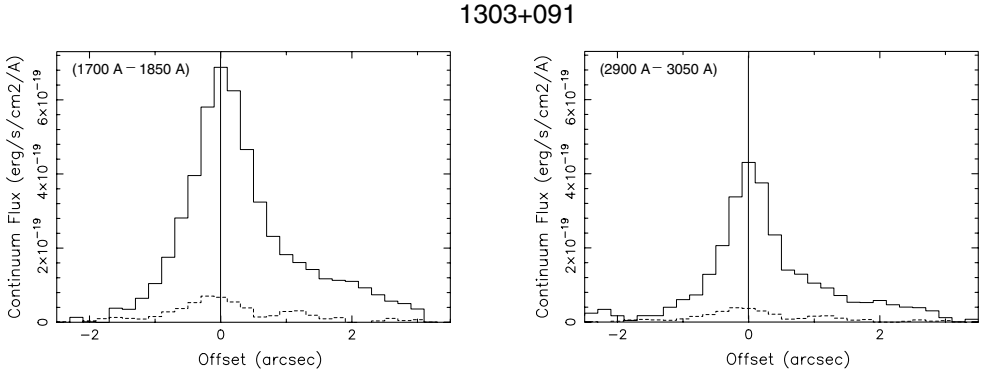

Figure 7. Spatial profiles of the line-free continuum emission (solid line) along the radio axis of 1303+091, between 1700–1850 Å rest-frame (left-hand panel) and between 2900–3050 Å rest-frame (right-hand panel). The dashed line shows the nebular continuum profile for the same wavelength ranges (see Section 6.1). South-east is to the left.

these values are not likely to be significant since that region coincides with the presence of strong sky emission lines, and thus it is very noisy. No comparison could be made between the electric vector orientation and the UV continuum axis because there are no rest-frame UV images available of 1303+091 to derive the UV axis.

5.2 The line emission

5.2.1 Emission-line structure

2D spectra of some of the main emission lines observed for 1303+091 are shown in the top panel of Fig. 9. These are C IV1548, He II 1640, C III] 1909, C II] 2326, [Ne IV] 2425 and [Ne V] 3426. The spatial profile along the radio axis of the emission line with the highest signal-to-noise ratio in both nuclear and extended regions (C III] in this case) was obtained, and it is presented in the same figure (bottom panel: top left). This profile was obtained in the same way as described for 0850–206 in Section 4.2.1, but for 1303+091 the spectral width of the C III] slice was 40 Å.

The detected C III] emission extends approximately 3.5 arcsec ($\sim$32 kpc) along the radio axis. The line emission is asymmetrically distributed with respect to the nucleus; in addition to the central nuclear peak, there is a fainter peak at approximately 1 arcsec ($\sim$9 kpc) to the north-west of the nucleus, close to the radio knot in the north lobe where the radio source appears to bend.

5.2.2 Emission-line kinematics

Kinematic information for the emission-line gas in 1303+091 was obtained following the same procedure as for 0850–206 (see Section 4.2.2). In this case, the emission line used for the analysis was the C III] 1909 line, which has the highest S/N ratio in the observed spectrum and a similar ionization state to [O II] 3727 used for 0850–206.

The spatial variation of the velocity centroids and linewidth of C III] along the radio axis of 1303+091 are presented in Fig. 9 (bottom panel: top right, bottom right).

The velocity shifts are referred to the velocity of the emission-line gas at the continuum centroid. In contrast with 0850–206, the overall velocity amplitude around the nucleus along the radio axis of 1303+091 changes by $\Delta v \lesssim 100$ km s^{-1} over $\sim$3 arcsec.

The C III] instrumentally corrected linewidths (FWHM) along the radio axis of 1303+091 are observed to vary between $\sim$600 km s^{-1}

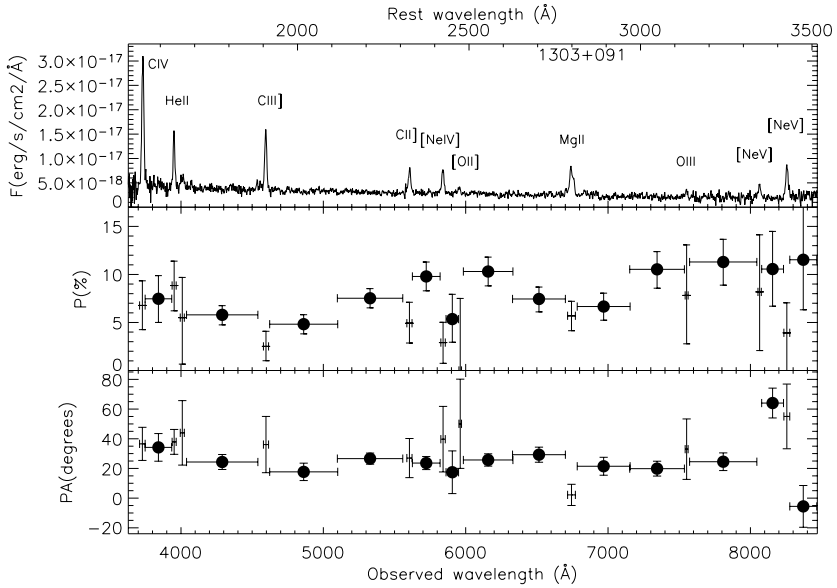

Figure 8. Spectral and polarization properties of the radio galaxy 1303+091. From top to bottom: the total flux spectrum, the observed fractional polarization and the position angle of the electric vector. Filled circles and crosses indicate, respectively, continuum bins and emission line bins with their underlying continuum.

at 2 arcsec north-west of the nucleus and 900 km s^{-1} at 1 arcsec south-east of the nucleus. The C III] linewidth at the location of the continuum centroid is found to be FWHM $\sim$ 800 km s^{-1}. It is interesting that the highest linewidths are measured at the location of the south-eastern inner radio knot, and that the narrowest lines are found outside the radio structure of the northern radio lobe (see Fig. 6). This is expected if the broadening of the emission lines is due to interactions with the radio structures.

5.2.3 Emission-line spectra

The total intensity spectrum of 1303+091 (corresponding to an aperture of 2 arcsec centred on the nucleus) is shown in Fig. 8 (top). In addition, integrated spectra of three regions defined along the radio axis (nuclear region, south-eastern and north-western EELR) are presented in Fig. 10 (see the figure caption for details of the apertures). The emission-line fluxes normalized to the C II] 2326 flux (see Section 4.2.3) for each region are listed in Table 6.

The spatial variation of the C III] 1909/C II] 2326 line ratio along the radio axis of 1303+091 is shown in Fig. 9 (bottom panel: bottom left). The nucleus presents the highest ionization state along the radio axis, with a line ratio C III]/C II] $\sim$ 2.5. There may be a second peak in the ionization state at $\sim$1.2 arcsec north-west of the continuum centroid. The emission-line gas with the lowest ionization is located at $\sim$1 arcsec south-east of the nucleus, with a ratio C III]/C II] $\sim$ 1.4. Interestingly, this region of low ionization presents the broadest emission lines (FWHM$_{\rm C\,III]}$ $\sim$ 950 km s^{-1}), and coincides with the location of a radio knot (see Fig. 6).

5.2.4 Polarization of the emission lines

Fig. 8 (middle plot) shows the observed fractional polarization for continuum and emission-line bins in 1303+091, for a spatial aperture of 2 arcsec centred on the continuum centroid. It can be noted that the polarization of the emission lines (with the underlying continuum) is similar or lower than the adjacent pure continuum bins. After subtracting the underlying continuum, the polarization of the stronger emission lines was measured. The permitted lines where found to be significantly polarized, $P_{\rm C\,IV} = 9.4^{+4.3}_{-4.1}$, $P_{\rm He\,II} = 11.7^{+4.4}_{-4.3}$ and $P_{\rm Mg\,II} = 5.6^{+2.6}_{-2.4}$ per cent (note that these values are for the entire emission line: there was an insufficient S/N ratio to attempt to separate any broad and narrow components). The low Galactic reddening towards 1303+091 means that the ISM in our Galaxy makes a negligible contribution to the polarization ($P_{\rm ISM} < 0.27$ per cent; Serkowski et al. 1975). The position angles of the electric vector for C IV and He II are 42° $\pm$ 13° and 36° $\pm$ 11°, respectively, which are almost perpendicular to the radio axis of 1303+091 (PA$_{\rm rad}$ $\sim$ 131°), suggesting that the polarization of C IV and He II (if real) is dominated by scattering. The electric vector orientation for Mg II is, however, found to be 167° $\pm$ 13°. This value is far from perpendicular to the radio axis, and it is probably affected by the low S/N ratio of the Mg II line.

The polarization of the stronger forbidden and semiforbidden lines was also measured, finding: $P_{\rm C\,III]} = 3.6^{+2.5}_{-2.4}$, $P_{\rm [Ne\,IV]} = 4.5^{+4.9}_{-4.5}$ and $P_{\rm [Ne\,V]} = 6.7^{+5.5}_{-6.7}$ per cent, all of which are consistent with zero.

6 DISCUSSION

6.1 The origin of the UV continuum

There is evidence that at least four mechanisms contribute to the UV excess observed in powerful radio galaxies (e.g. Tadhunter et al. 2002, and references therein); these are: scattered AGN light, young stellar population, nebular continuum and direct AGN light. In this section the relative contribution of the different components to the UV continuum of 0850–206 and 1303+091 is investigated.

Direct AGN light is found to contribute significantly to the UV continuum of a source only when broad permitted lines are detected in the intensity spectrum. Such sources are likely to be partially obscured, or low luminosity, quasars and they usually present low levels of polarization of the order of $\lesssim$4 per cent (e.g. Stockman, Angel & Miley 1979; Antonucci 1984). In the cases of 0850–206 and 1303+091, no broad components are detected in the profiles of the permitted emission lines in their spectra; also, for both galaxies the

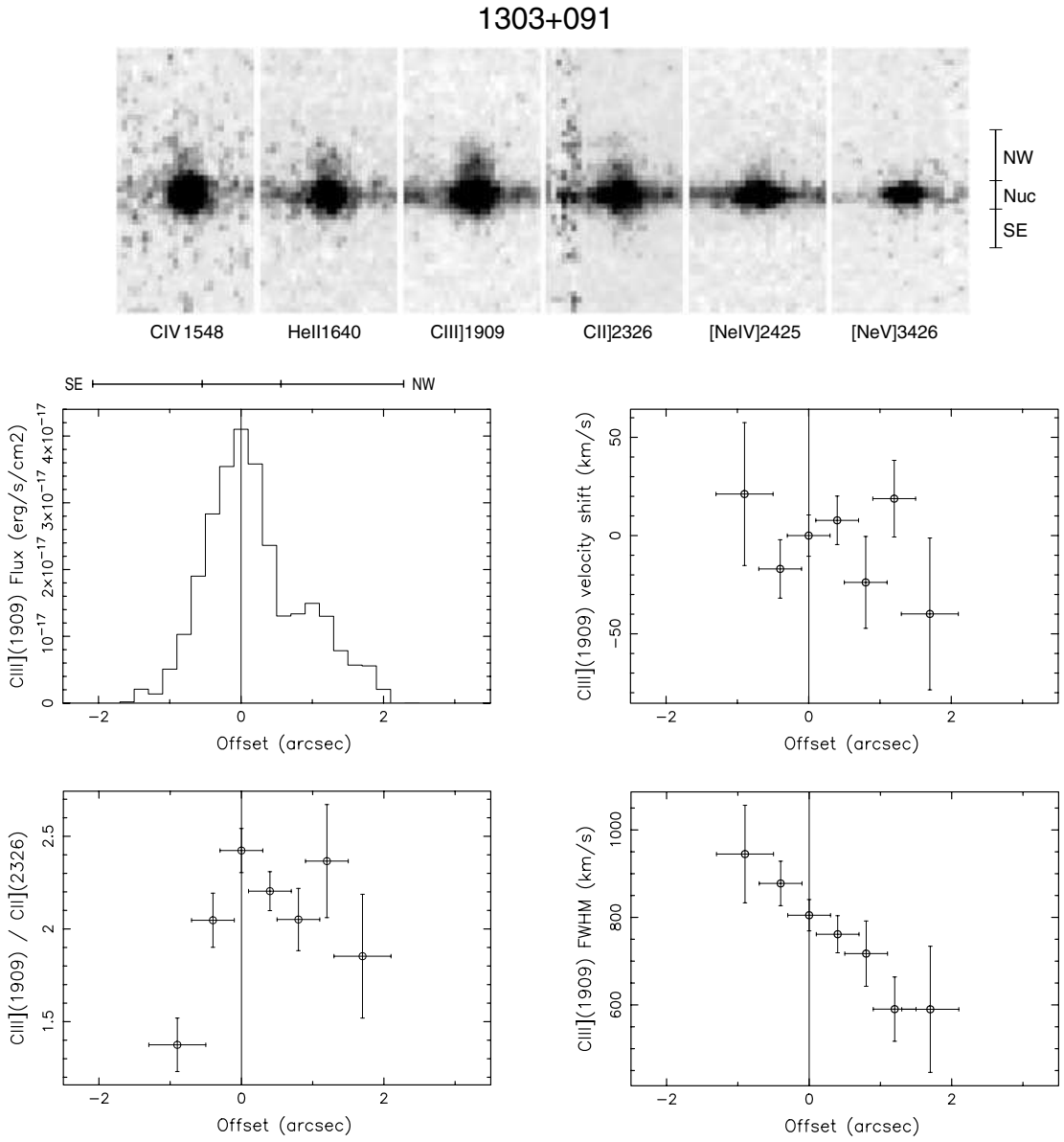

Figure 9. Top panel: 2D spectra of the main emission lines for 1303+091. Each spectrum covers 9.6 arcsec along the radio axis, and 29 Å (rest-frame) in the spectral direction. The regions defined along the slit are indicated by the solid line at the right of the panel. Bottom panel: emission-line spatial analysis along the radio axis of 1303+091. Top left: spatial variation of the C III] 1909 flux. The spatial regions defined along the slit are indicated by a solid line at the top of the plot. Bottom left: spatial variation in the C III] 1909/C II] 2326 line ratio. Top right: spatial variation in the C III] 1909 velocity centroids. Bottom right: spatial variation of the C III] 1909 linewidth. South-east is to the left in the four plots.

observed polarization is on average $\gtrsim$8 per cent. In addition to this, inspection of the broad-band images of 0850–206 and 1303+091 shows no evidence for a point source in the nucleus of either galaxy. Direct AGN light is therefore not an important mechanism in the UV continuum of 0850–206 or 1303+091. Thus, nebular emission, young stars and scattered AGN light will be the main mechanisms contributing to the UV continuum emission of both sources.

The theoretical nebular continuum for Case B recombination (Osterbrock 1989) can be derived from the strength of the recombination lines, Hβ in particular. As the observed wavelength range for 0850–206 and 1303+091 did not cover the Hβ line, the nebular continuum emission of these galaxies was instead derived by using the recombination line He II 1640 and the average line ratio He II/Hβ $\sim$3.18 given by McCarthy (1993) for radio galaxies. The spatial profiles of the nebular continuum emission for 0850–206 and 1303+091 are shown in Figs 2 and 7, respectively. To calculate these profiles, a slice perpendicular to the dispersion direction, of 40-Å width in the observed frame, containing the He II emission line was extracted from the total two-dimensional spectrum of each galaxy. Then, adjacent line-free continuum slices were extracted, combined and scaled to have the same spectral width as the He II slice. The combined continuum slice was then subtracted from the He II slice to produce a continuum-free He II spatial profile, which was used to generate the nebular continuum emission profile (using the task NEBCONT in DIPSO). For both sources, the nebular contribution is generally more important in the extended regions than in the nucleus. In 0850–206, essentially all of the light south of 2 arcsec from the nucleus is nebular emission. For the apertures used in

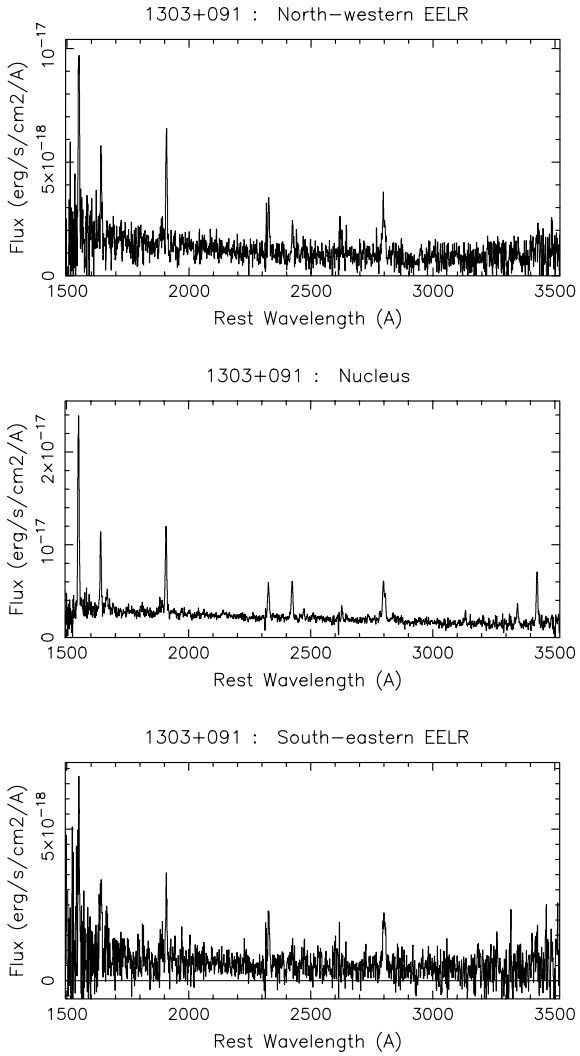

Figure 10. Integrated spectra for the different emission-line regions in 1303+091 defined along the radio axis: north-western EELR (top; 1.8 × 1.0 arcsec^2 aperture centred at 1.4 arcsec NW of the continuum centroid), nucleus (middle; 1.0 × 1.0 arcsec^2 aperture centred on the continuum centroid) and south-eastern EELR (bottom; 1.6 × 1.0 arcsec^2 aperture centred at 1.3 arcsec SE of the continuum centroid).

the polarization analysis, the contribution of the nebular continuum to the total continuum emission in 0850–206 is found to be ∼22 per cent for the rest-frame wavelength range 1700–1850 Å, and ∼11 per cent for the rest-frame range 2900–3050 Å. In the case of 1303+091, the nebular contribution is ∼11 per cent for both rest-frame wavelength ranges 1700–1850 and 2900–3050 Å. Thus, at least ∼80 per cent of the UV continuum in these galaxies will be a combination of stellar light and scattered AGN light.[2] It is likely that if the continuum polarization of the source is low, the contribution of a young stellar population will be important. On the other hand, if it is the case that the observed continuum polarization is high, then the scattered quasar light will probably dominate the UV continuum emission of the source.

[2] The stellar light will include both the old stellar population of the galaxy and any young stellar population. Based on *K*-magnitudes at these redshifts (*K*-*z* relation; e.g. McCarthy 1993), the old stellar population is likely to contribute $\lesssim$10 per cent of the light at 3000 Å, and will be negligible at wavelengths <2500 Å.

Table 6. Emission-line integrated fluxes (corrected for Galactic reddening and normalized to the C II] 2326 flux) for the different regions in 1303+091. The details of the apertures are in the caption of Fig. 10. The quoted errors correspond to the line fitting errors.

1303+091 Line	SE EELR (1.3 arcsec SE)	Nucleus	NW EELR (1.4 arcsec NW)
C IV1548	2.10 ± 0.33	4.84 ± 0.20	3.06 ± 0.32
He II 1640	1.59 ± 0.36	1.71 ± 0.11	1.40 ± 0.24
O III] 1666	–	0.53 ± 0.12	–
[Mg VI] 1806	–	0.16 ± 0.04	–
Si III] 1882	–	0.22 ± 0.04	–
Si III] 1892	–	0.23 ± 0.04	–
C III] 1909	1.08 ± 0.13	2.28 ± 0.09	1.89 ± 0.17
N II] 2139	–	0.09 ± 0.02	–
C II] 2326	1.00 ± 0.08	1.00 ± 0.04	1.00 ± 0.08
[Ne IV] 2425	–	1.09 ± 0.05	0.55 ± 0.09
[O II] 2472	–	0.20 ± 0.03	–
[Mg VII] 2510	–	0.11 ± 0.02	–
[Mg VII] 2629	–	0.27 ± 0.03	–
He II 2733	–	0.12 ± 0.02	–
[Mg V] 2783	0.18 ± 0.08	0.21 ± 0.04	0.30 ± 0.14
Mg II 2800	1.39 ± 0.17	1.70 ± 0.07	1.30 ± 0.17
O III 2836	–	0.13 ± 0.02	0.23 ± 0.17
O III 3133	–	0.26 ± 0.04	–
He II 3203	–	0.14 ± 0.04	–
[Ne V] 3346	–	0.54 ± 0.05	–
[Ne V] 3426	–	1.45 ± 0.08	<0.67
C II] 2326 flux (10^{-17} erg s^{-1} cm^{-2})	3.71 ± 0.30	7.10 ± 0.25	4.32 ± 0.34

The relative contributions of the continuum components can be roughly quantified by assuming that the observed fractional polarization $P_{\rm obs}$ is diluted by unpolarized radiation, which is mainly composed of nebular continuum emission $F_{\rm neb}$ and stellar light $F_{\rm star}$. Thus we can use the following equation:

$$P_{\rm obs} = P_{\rm o} \times \frac{F_{\rm scatt}}{F_{\rm scatt} + F_{\rm neb} + F_{\rm star}}, \quad (1)$$

where $P_{\rm o}$ is the intrinsic undiluted polarization and $F_{\rm scatt}$ is the scattered AGN flux. Assuming that dust scattering is the dominant mechanism for 0850–206 and 1303+091 (see Section 6.1.1 below for a discussion concerning the scatterers), and taking into account that Zubko & Laor (2000) showed that polarization is almost independent of optical depth, the calculations derived by Manzini & di Serego Alighieri (1996) for optically thin dust scattering can be used to obtain a good estimate of the intrinsic polarization of the scattered radiation. Their model uses the geometry indicated by the unified schemes for radio sources (Barthel 1989) and assumes that the nuclear radiation is emitted along two diametrically opposed cones with a half-opening angle of 45°. Depending on the angle between the cone axis and the line of sight, the observed intrinsic polarization for a given wavelength will vary. Using equation (1) and assuming that the observer's viewing angle relative to the cone axis varies between 50° and 90°, the approximate contributions of the different components to the continuum emission of 0850–206 and 1303+091 can be estimated for the rest-wavelengths ranges 1700–1850 and 2900–3050 Å. The results are listed in Table 7.

In the case of 0850–206 the contribution of young stellar population is negligible or null, and the scattered AGN light dominates the

Table 7. Approximate relative contributions of the nebular continuum $F_{\rm neb}$, stellar population $F_{\rm star}$ and scattered AGN light $F_{\rm scatt}$ to the total continuum emission of 0850–206 and 1303+091 in the rest wavelength ranges 1700–1850 and 2900–3050 Å, evaluated for a 2 arcsec wide aperture centred at the continuum centroid of the galaxies. Also are given the ranges of intrinsic continuum polarization $P_{\rm o}$ for dust scattering, assuming a half-cone opening angle of 45° and angles between the cone axis and the line of sight in the range 50°–90° (Manzini & di Serego Alighieri 1996), together with the observed polarization $P_{\rm obs}$ in the two wavelength ranges.

Source	λ range (Å)	$P_{\rm o}$ (per cent)	$P_{\rm obs}$ (per cent)	$F_{\rm neb}$ (per cent)	$F_{\rm star}$ (per cent)	$F_{\rm scatt}$ (per cent)
0850–206	1700–1850	6–16	23 ± 3	∼22	∼0	∼78
	2900–3050	6–17	15.6 ± 1.3	∼11	∼0	∼89
1303+091	1700–1850	6–16	6.2 ± 1.2	∼11	∼0–50	∼39–89
	2900–3050	6–17	10.1 ± 1.7	∼11	∼0–29	∼60–89

continuum emission, with a relative contribution of ∼80–90 per cent depending on the nebular contribution for the different wavelength ranges. Based on the results obtained for observer's viewing angles of 50° and 90° using equation (1), it is likely that the angle between the radio axis and the line of sight for 0850–206 is close to 90°, given that for angles below 90° the resulting unpolarized contribution is negative (particularly in the 1700–1850 Å range). This orientation is also consistent with the radio image of this galaxy (see Fig. 1).

On the other hand, in the case of 1303+091, the stellar population can account for up to 50 per cent of the continuum emission if the radio axis is on the plane of the sky, or its contribution could be null if the angle between the line of sight and the radio axis is close to 50°.

An alternative analysis consists of fitting the spectra of both galaxies with four components: nebular continuum, scattered quasar light, young stellar population and old stellar population. The quasar spectrum used for the fits was a radio-loud quasar composite (from Telfer et al. 2002; with a power-law index $\alpha_\nu = -0.67$ for rest-frame wavelengths $\lambda \gtrsim 1300$ Å, and derived using over 200 spectra taken with the *Hubble Space Telescope*, with redshifts $z > 0.33$). The quasar spectrum was then scattered using Zubko & Laor (2000) dust scattering models, both optically thin and optically thick (see Section 6.1.1). Both old and young stellar populations were modelled using the 2000 version of the GISSEL codes of Bruzual & Charlot (cf. Bruzual & Charlot 1993, 2003), assuming a Salpeter IMF, solar metallicity and instantaneous burst models of age 4 Gyr and 10 Myr (approximate age of the radio source), respectively. The nebular continuum contribution was fixed by our observations and the other three components were allowed to vary. Another variable was included in the fit to account for any plausible intrinsic reddening in each galaxy.

The result of the fits is shown in Fig. 11. The best fit in both cases was obtained when the quasar spectrum had been scattered by optically thin dust, and for both galaxies a small intrinsic reddening was required: $E^{\rm intrin}_{B-V} = 0.087$ for 0850–206, $E^{\rm intrin}_{B-V} = 0.020$ for 1303+091. This intrinsic reddening could plausibly be due to the same dust that is causing the scattering. The contribution of old stellar population in the best-fitting model is consistent at K-band wavelengths with typical K-band magnitudes for $z \sim 1.4$ radio galaxies (see the K-z relation; McCarthy 1993). The fits are good in general apart from the wavelength region ∼2000–2200 Å, where the fit underpredicts the observed continuum emission (for further discussion see Section 6.1.1). The results from the fitting show that in 0850–206 the scattered quasar light dominates the UV continuum emission and there is no requirement at all for a young stellar component; whilst in the case of 1303+091, both scattered quasar light and young stellar population have important contributions to the UV light: in the wavelength range 1700–1850 Å contributions are comparable, while in the 2900–3050 Å range scattered quasar light contributes more than 50 per cent. These results are in complete agreement with our calculation above (see Table 7).

Characteristic photospheric absorption features of OB stars, such as S V1502 and N IV1720, were searched for in the spectra of both sources, especially in 1303+091, where the contribution of a young stellar population is suspected to be significant. No clear evidence for any of these absorption lines was found in any of the spectra,

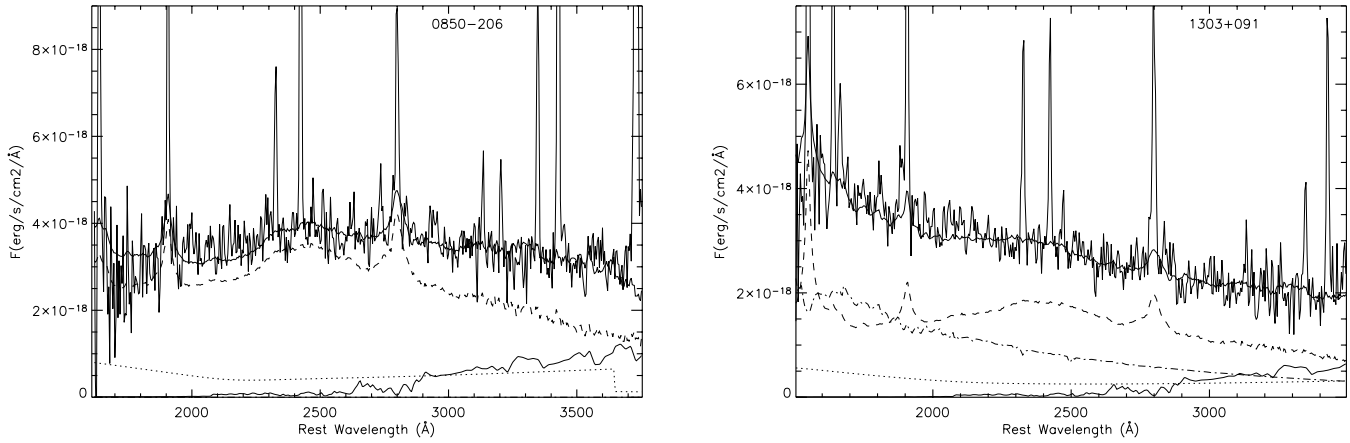

Figure 11. Four-component fit to the spectra of 0850–206 (left-hand panel) and 1303+091 (right-hand panel). The components of the fit include: nebular continuum (dotted line), dust-scattered radio-loud quasar light (dashed line), young stellar population (dot-dash-dot line) and old stellar population (thin solid line). The total fit is indicated by a thick solid line. Both the 0850–206 and 1303+091 spectra have been smoothed into 4-Å (rest-frame) bins.

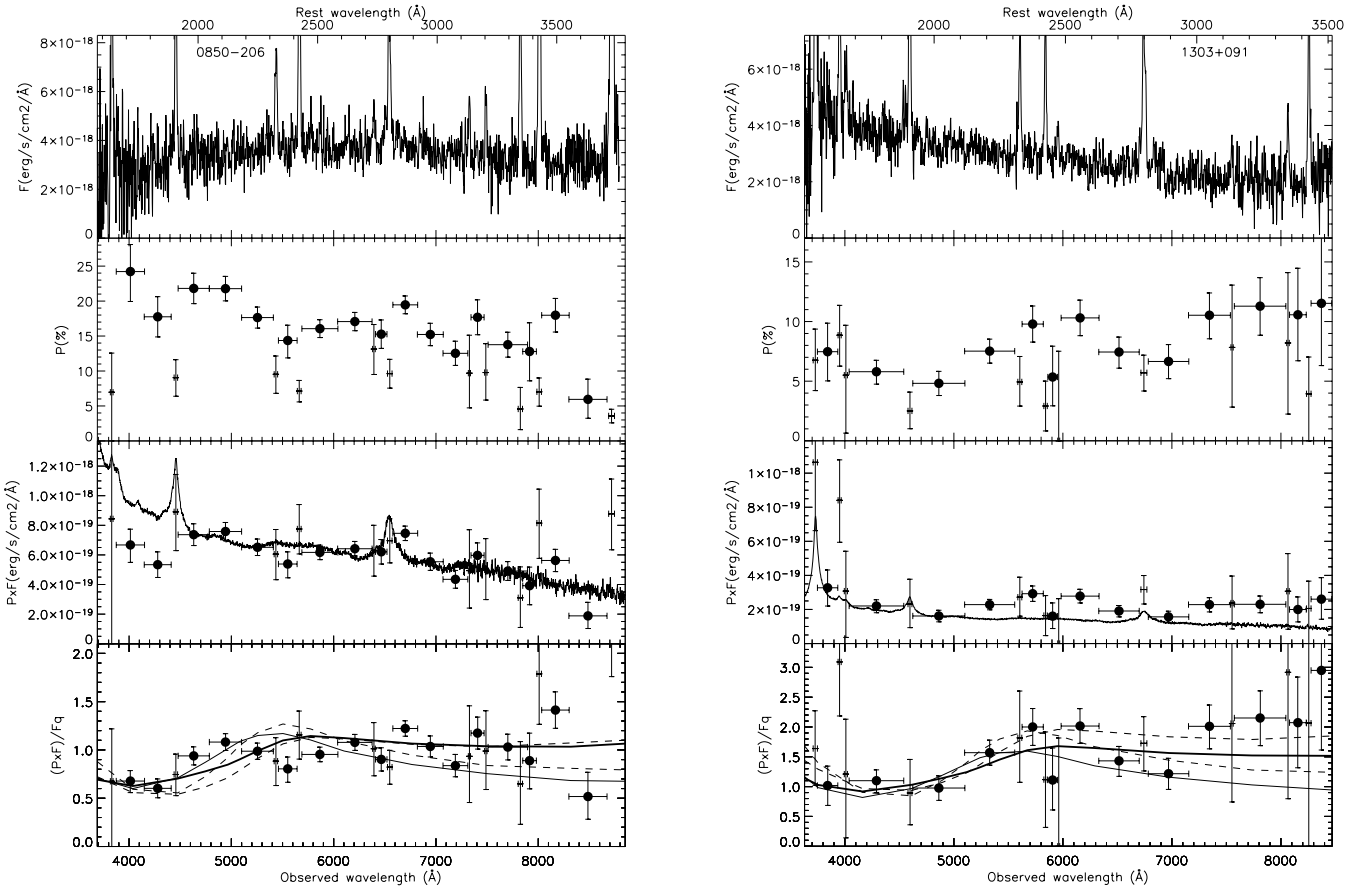

Figure 12. Polarization properties of 0850–206 (left-hand panel) and 1303+091 (right-hand panel). For each panel, from top to bottom: the unsmoothed total flux spectrum in an expanded scale to show the continuum, the observed fractional polarization, the polarized flux with a composite radio-loud quasar spectrum (from Telfer et al. 2002, normalized to the polarized flux at rest-frame 2000 Å) superimposed, and the ratio between the polarized flux spectrum and the composite quasar spectrum with the Zubko & Laor (2000) models overplotted [for optically thin (thin lines) and optically thick (thick lines) dust cases, with scattering angles of 90° (solid lines) and 120° (dashed lines)]. Filled circles and crosses indicate, respectively, continuum bins and emission line bins with their underlying continuum.

although the S/N ratio of the spectra is insufficient for their absence to rule out a young stellar population.

6.1.1 The nature of the scatterers

The nature of the scattering material in high-redshift radio galaxies is an important question, still under debate. Both electrons (Fabian 1989) and dust grains (Tadhunter et al. 1988) have been proposed as possible scattering agents; but dust is generally preferred, mainly because of the greater scattering efficiency of dust grains over electrons. Polarization observations of radio galaxies show that for the implied scattered light to be fully scattered by electrons, the required mass of ionized gas is very large ($\sim 10^{10}$–10^{12} $M_{\odot}$; e.g. di Serego Alighieri, Cimatti & Fosbury 1994; Cimatti et al. 1996). Thus, although some light might be scattered by electrons (mainly in the central regions), the scattering process is likely to be dominated by the dust grains (provided that some dust is present).

Zubko & Laor (2000) present detailed calculations of the scattering and polarization properties of light scattered by both optically thin and optically thick dust, using the Mathis, Rumpl & Nordsieck (1977) Galactic dust model. They find that the spectrum of the scattered light is quite different in the two cases. In the optically thin case the emergent scattered spectrum is bluer than the incident one for $\lambda > 2200$ Å, and it has a broad dip centred at $\lambda \sim 1500$ Å. In the optically thick case the emergent spectrum is generally grey scattered for $\lambda > 2200$ Å, and shows a drop at $\lambda < 2200$ Å. Although the total scattered intensity depends on optical depth, the polarization of the scattered light varies with wavelength in a very similar way for both optically thin and optically thick cases. The polarization tends to decrease slightly from 10 000 to ∼2000 Å, shows a dip centred at ∼1800 Å, and then tends to increase sharply towards the far-UV.

In the case of quasar light scattered by electrons, the emergent spectrum will be similar to the incident one, since the Thomson scattering cross-section is independent of wavelength. Thus, for $\lambda >$ 2200 Å, optically thick dust scattering can mimic electron scattering.

In Fig. 12 continuum polarization properties of 0850–206 (left-hand panel) and 1303+091 (right-hand panel) are presented. In each panel, from top to bottom the following are plotted: the total flux spectrum, the observed fractional polarization, the polarized flux with a composite radio-loud quasar spectrum (from Telfer et al. 2002) superimposed, and the ratio between the polarized flux spectrum and the composite quasar spectrum. The dust-scattering predictions from Zubko & Laor (2000) are overplotted on this bottom plot (see the caption for details).

This composite quasar spectrum can be considered to be an average quasar spectrum, and thus it can be compared with the polarized flux spectra of 0850–206 and 1303+091 (Fig. 12). It is found that,

for both galaxies, the polarized spectrum is slightly redder than the incident one, which is in agreement with spectropolarimetric studies of other high-redshift radio galaxies (e.g. Cimatti et al. 1996; Kishimoto et al. 2001). The ratio between polarized and incident spectra can be directly compared with the scattering efficiency × intrinsic polarization (cf. Equation 1); the dust scattering predictions of Zubko & Laor (2000) were used for this comparison. It can be seen that the broad dip shortward of ∼2200 Å (rest-frame) predicted by both optically thin and optically thick dust models is found in both galaxies, more pronounced in 1303+091. It therefore appears that dust dominates the scattering process in both 0850–206 and 1303+091.

The detection of features in the scattered light spectrum around 2200 Å is particularly interesting when compared with the extinction laws of different galaxies. The extinction curve of the Milky Way shows a strong 2200-Å dust feature; this feature is less pronounced for the Large Magellanic Cloud, is even weaker for the Small Magellanic Cloud, and is entirely absent in nearby starburst galaxies (e.g. Calzetti, Kinney & Storchi-Bergmann 1994). These differences are likely to be related to the metallicity of the galaxy and the composition of the dust. The fact that a 2200-Å dust feature is detected in the total flux spectra (Fig. 11) and even more strongly in the polarized flux spectra (Fig. 12) of the two radio galaxies studied in this paper, implies that the dust in these distant galaxies is different in nature or composition to that of nearby starburst galaxies, and is much more comparable to Galactic dust. On the other hand, the fits to the total continuum spectra (Fig. 11) show that, although the observed continuum and the model have the same shape around in the wavelength range ∼2000–2200 Å, the model (which uses a Galactic dust scattering prediction) slightly underpredicts the continuum emission in this range. This suggests that the 2200-Å feature is not as strong as in the models, and that the dust in these galaxies, although similar, may not be exactly the same as Galactic dust.

6.2 Ionization of the emission-line regions

In the above sections where the results are described, the spatial variation of the line ratio C III] 1909/C II] 2326 along the position of the slit for 0850–206 and 1303+091 were presented. For 1303+091 it was found that the ionization state peaks in the nuclear region, with a possible second peak at ∼1.2 arcsec to the north-west of the nucleus. For 0850–206 the highest ionization state was found ∼0.5 arcsec offset of the nucleus to the north, then it decreases at both sides of this location.

In order to study in more detail the ionization state of the emission-line gas in the two galaxies, the line ratios (derived from the total intensity spectra) for the different regions have been compared with theoretical predictions of several ionization models. The resulting diagnostic diagrams are presented in Fig. 13, which involve the following line ratios: C III] 1909/He II 1640, C III]1909/C II] 2326, and [Ne IV] 2425/[Ne V] 3426. The points correspond to the different emission-line regions defined along the slit (for details of the apertures see the captions of Figs 5 and 10).

The data are compared with the following ionization models: (i) optically thick power-law photoionization, with spectral indices $\alpha = -1.0$ and -1.5 (solid lines); (ii) photoionization including matter-bounded clouds (dot-dash-dot line); (iii) shock-ionization, with shock velocities in the range $200 \leqslant v \leqslant 500$ km s^{-1} (dashed grid); and (iv) shock-ionization including a photoionized precursor (dotted grid). For details concerning how the different models were generated, see Solórzano-Iñarrea et al. (2001) and references therein.

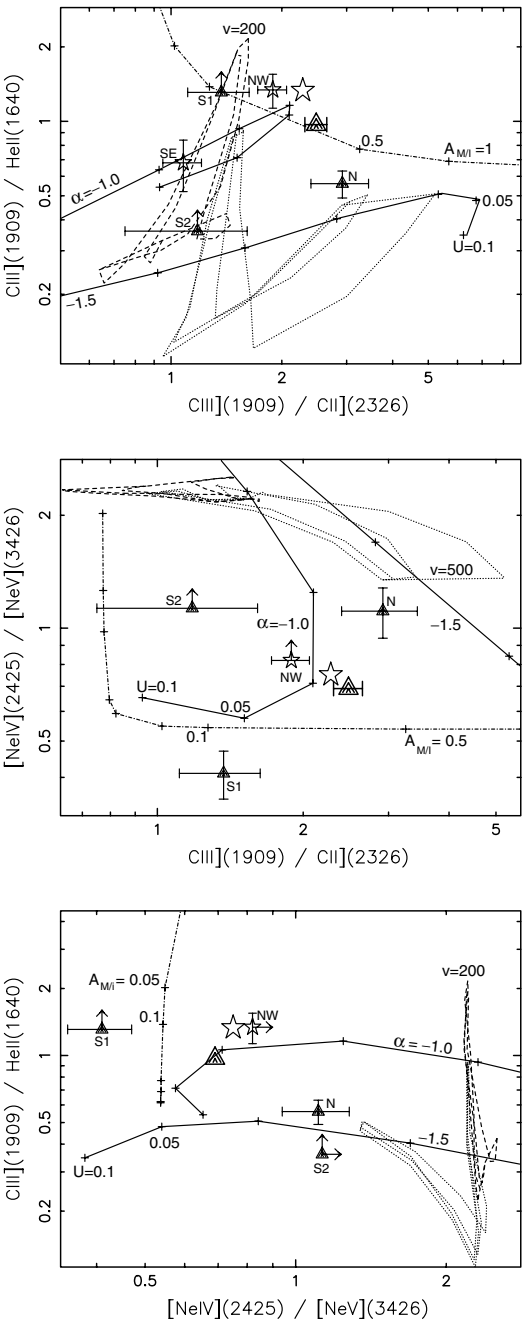

Figure 13. Diagnostic diagrams for different regions in 0850–206 (triangles) and 1303+091 (stars). Bigger symbols indicate the nucleus, smaller ones denote EELR. Solid lines represent optically thick single-slab power-law ($F_\nu \propto \nu^\alpha$) photoionization models (MAPPINGS) with $\alpha = -1.0, -1.5$ and a sequence in ionization parameter ($2.5 \times 10^{-3} < U < 10^{-1}$). The dot-dash-dot line corresponds to photoionization models including matter-bounded clouds ($10^{-2} \leqslant A_{\rm M/I} \leqslant 10$; Binette, Wilson & Storchi-Bergmann 1996). Shock (dashed grid) and shock+precursor (dotted grid) models are included (Dopita & Sutherland 1996); each sequence corresponds to a fixed magnetic parameter ($B/\sqrt{n} = 0, 1, 2, 4\ \mu$ Gcm$^{-3/2}$) and changing shock velocity ($200 \leqslant v \leqslant 500$ km s^{-1}).

By comparing the three diagnostic diagrams, it can be seen that the points of the nuclear regions (bigger symbols) of the two galaxies fall close together in the three diagrams, indicating that they have a similar state of ionization. Both nuclei are well reproduced by the

photoionization predictions with $\alpha \sim -1.0$ and $U \sim 0.025$. Note that they could also be explained by the mixed-medium photoionization models, since these models can be slightly tuned to better fit the data. The shock-ionization predictions, however, clearly fail to reproduce the ionization state of the nuclear regions in the two galaxies.

The EELR of 1303+091 (open stars) are well explained by the photoionization models with $\alpha \sim -1.0$, although the data can also be consistent with low velocity shock-ionization predictions. Note, however, that in the middle and lower diagrams there is no data for the SE region, since none of the neon lines was measurable in this region and therefore the ratio [Ne IV]/[Ne V] could not be calculated. Only a lower limit could be derived for the same line ratio for the NW region. Thus, the ionization of the EELR in 1303+091 cannot be well constrained.

The EELR of 0850–206 (triangles) fall well apart from each other in the diagrams. Whilst the ionization of the northern region N can be explained by $\alpha \sim -1.5$ photoionization predictions and by shock + precursor models with shock velocities of ∼500 km s^{-1}, the southern region S1 is best explained by mixed-medium photoionization models with $0.05 < A_{\rm M/I} < 0.1$. On the other hand, the ionization of the outermost southern region S2 is poorly constrained and thus can be reproduced by either the photoionization models or shock-ionization predictions with or without a precursor gas.

In summary, it is found that the ionization state of the nuclear regions in the two galaxies can only be reproduced by photoionization predictions. The photoionization models give also reasonable fits to the data of the extended regions. However, their ionization is less constrained, and with the exception of the S1 region in 0850–206, the ionization of which is only consistent with the mixed-medium photoionization models, the ionization of the other EELR could also be explained by shock-ionization predictions. In particular, the SE region of 1303+091, which coincides with the location of a radio knot, was found to have the lowest ionization state and the highest emission linewidths; these features are expected when the gas is perturbed by strong interactions with the radio source structures (e.g Clark et al. 1998).

6.3 Variations with radio source size

Clearly, continuum studies of only two sources are not enough to draw significant conclusions concerning the evolution of the continuum properties of radio galaxies with radio source age. Nevertheless, the results presented in this paper are in line with what might have been expected.

If a jet-induced starburst occurs when the radio hotspots pass through the host galaxy, by a few times 10^7 yr later (typical age of a radio source) the starburst luminosity will have decreased to ∼10 per cent of its peak value (Best et al. 1996). Therefore, the presence of a young stellar population, possibly jet-induced, may dilute the scattered AGN light in smaller (younger) radio sources and, consequently, the observed continuum polarization would be lower. On the other hand, for larger (older) radio sources, in which the contribution of a starburst to the total optical flux will be dramatically decreased, the scattered AGN light dominates the UV continuum emission. Our findings are consistent with this scenario. 0850–206, the larger radio source of the two ($D_{\rm rad} \sim 118$ kpc), presents a high continuum polarization, averaging ∼17 per cent; scattered quasar light dominates the UV continuum emission and the starlight contribution is null or negligible. In contrast, 1303+091 ($D_{\rm rad} \sim 73$ kpc) presents a lower continuum polarization, averaging ∼8 per cent, and in this galaxy the young stellar population could account for up to ∼50 per cent of the UV continuum emission.

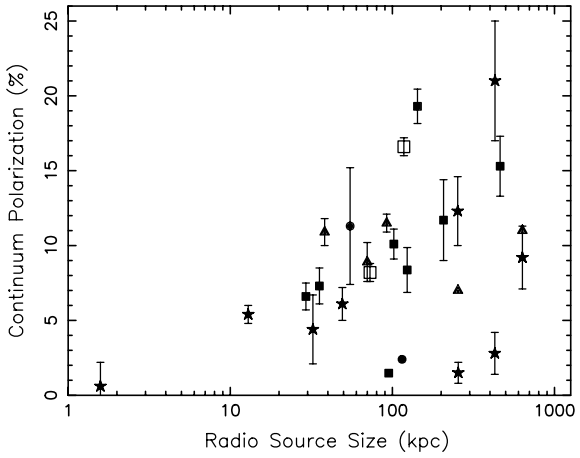

Figure 14. Observed fractional continuum polarization of high-redshift radio galaxies versus their radio source size. Different symbols indicate different redshift ranges: $0.5 < z < 1.0$ (filled stars), $1.0 < z < 2.0$ (filled triangles), $2.0 < z < 3.0$ (filled squares) and $3.0 < z < 4.0$ (filled circles). Also plotted are the two radio galaxies from our sample presented in this paper (big open squares). The data corresponding to the other galaxies have been taken from di Serego Alighieri et al. (1989, 1993, 1996); Tadhunter et al. (1992); Cimatti et al. (1993, 1996, 1997); Dey & Spinrad (1996); Dey et al. (1997) and Vernet et al. (2001). Information concerning the sizes of radio sources has been obtained from Dunlop et al. (1989); McCarthy, van Breugel & Kapahi (1991); Röttgering et al. (1994); Carilli, Owen & Harris (1994); Carilli et al. (1997); Cohen et al. (1997) and Kapahi et al. (1998).

These results can be combined with those of previous polarization studies of high-redshift radio galaxies, in order to explore if there is any correlation between continuum polarization and size of the radio source. Fig. 14 shows the fractional continuum polarization versus radio source size for a sample of high-redshift radio galaxies taken from the literature (see the figure caption for details). It must be emphasized that this set of radio galaxies consists of several different subsamples, many of which are biased (e.g. towards high polarization objects). In addition, these samples are at different redshifts, making the wavelength range studied different and bringing evolution effects into play, thus making the objects not directly comparable. However, even despite this, it is intriguing that there is a hint of a weak correlation between polarization and radio source size (Spearmann–Rank test gives a 97 per cent significance level): smaller radio sources do not show high polarizations, and the larger the radio source the higher its polarization can be.

The relation between radio source size and polarization will be better tested when our full sample of radio galaxies at the same redshift ($z \sim 1.4$), with a large range of radio sizes, has been observed. Also, it will be interesting to sum the spectra of the smaller radio sources in the full sample, with similar characteristics to 1303+091, to search at higher S/N ratio for photospheric absorption features of OB stars, which would directly prove the presence of a young stellar population.

7 SUMMARY AND CONCLUSIONS

This paper presents the results obtained from VLT spectropolarimetric observations of two powerful radio galaxies at $z \sim 1.4$. Analysis of their scattered flux spectra and their polarization properties indicates that the scattering process in these galaxies is dominated by dust, the 2200-Å feature of which suggests that it is similar to Galactic dust in nature. The larger radio source (0850–206) presents

a continuum fractional polarization reaching as high as ∼24 per cent at ∼2000 Å (rest-frame). For this galaxy, scattered AGN light must dominate the UV continuum, the nebular emission contributes up to ∼22 per cent and there is no requirement for any young starlight contribution. The smaller radio source (1303+091) presents a lower continuum polarization averaging ∼8 per cent across the observed wavelength range, and its nebular continuum contribution to the UV continuum is ∼11 per cent. For this galaxy, the starlight could contribute between 0 and 50 per cent, depending on the radio axis orientation, with multicomponent fit to the spectral energy distribution favouring the upper end of this range. In both galaxies, the position angle of the electric vector is almost independent of wavelength and within 15° of perpendicular to the radio axis.

The emission-line properties of the galaxies are also analysed. Illumination by the central AGN is likely to be the dominant ionization mechanism of the nuclear and EELR in both galaxies, although the region coincident with the radio knot in 1303+091 shows features reminiscent of jet-cloud interactions.

A compilation of polarimetric observations from the literature shows hints of a correlation between continuum polarization and radio source size, albeit for incomplete and biased samples. This is broadly in line with what might have been expected; that in smaller radio sources the presence of a young stellar population (possibly jet-induced) may dilute the scattered AGN light, while in larger (older) radio sources the presence of young stars is negligible and the scattered AGN light dominates the UV continuum. It is clearly necessary to observe and analyse the rest of our sample to confirm this result with a complete and unbiased sample, in order to allow significant conclusions to be drawn concerning the evolution of the continuum properties of radio galaxies with radio source size.

ACKNOWLEDGMENTS

We are very grateful to Joel Vernet for kindly providing his IDL spectropolarimetric reduction code and to Carlos De Breuck for providing his modified version of the code and for a constructive discussion concerning reduction of VLT spectropolarimetric data. We are also indebted to Viktor Zubko for kindly supplying us with the results of their dust scattering models in digitized form. CSI thanks Makoto Kishimoto for useful discussions. We also thank the anonymous referee for a careful reading of the manuscript and useful comments that helped to improve the paper. This work is based on observations made at the European Southern Observatory, Paranal, Chile. This research has made use of the NASA/IPAC Extragalactic Data base (NED) which is operated by the Jet Propulsion Laboratory, California Institute of Technology, under contract with the National Aeronautics and Space Administration. The authors acknowledge the data analysis facilities provided by the Starlink Project which is run by CCLRC on behalf of PPARC. This research has also made use of the USNOFS Image and Catalogue Archive operated by the United States Naval Observatory, Flagstaff Station (http://www.nofs.navy.mil/data/fchpix/).

REFERENCES

Antonucci R.R.J., 1984, ApJ, 278, 499
Antonucci R.R.J., Miller J.S., 1985, ApJ, 297, 621
Athreya R.M., Kapahi V.K., McCarthy P.J., van Breugel W., 1997, MNRAS, 289, 525
Barthel P.D., 1989, ApJ, 336, 606
Baum S.A., Heckman T.M., Bridle A., van Breugel W.J.M., Miley G.K., 1988, ApJS, 68, 643
Best P.N., Longair M.S., Röttgering H.J.A., 1996, MNRAS, 280, L9
Best P.N., Longair M.S., Röttgering H.J.A., 1998, MNRAS, 295, 549
Best P.N., Eales S.A., Longair M.S., Rawlings S., Rottgering H.J.A., 1999a, MNRAS, 303, 616
Best P.N., Röttgering H.J.A., Lehnert M.D., 1999b, MNRAS, 310, 223
Best P.N., Röttgering H.J.A., Longair M.S., 2000a, MNRAS, 311, 23
Best P.N., Röttgering H.J.A., Lehnert M.D., 2000b, MNRAS, 315, 21
Best P.N., Peacock J.A., Brookes M.H., Dowsett R.E., Röttgering H.J.A., Dunlop J.S., Lehnert M.D., 2003, MNRAS, 346, 1021
Binette L., Wilson A.S., Storchi-Bergmann T., 1996, A&A, 312, 365
Bruzual G., Charlot S., 1993, ApJ, 405, 538
Bruzual G., Charlot S., 2003, MNRAS, 344, 1000
Calzetti D., Kinney A.L., Storchi-Bergmann T., 1994, ApJ, 429, 582
Carilli C.L., Owen F.N., Harris D.E., 1994, AJ, 107, 480
Carilli C.L., Roettgering H.J.A., van Ojik R., Miley G.K., van Breugel W.J.M., 1997, ApJS, 109, 1
Cimatti A., di Serego-Alighieri S., Fosbury R.A.E., Salvati M., Taylor D., 1993, MNRAS, 264, 421
Cimatti A., de Serego Alighieri S., Field G.B., Fosbury R.A.E., 1994, ApJ, 422, 562
Cimatti A., Dey A., van Breugel W., Antonucci R., Spinrad H., 1996, ApJ, 465, 145
Cimatti A., Dey A., van Breugel W., Hurt T., Antonucci R., 1997, ApJ, 476, 677
Clark N.E., Axon D.J., Tadhunter C.N., Robinson A., O'Brien P., 1998, ApJ, 494, 546
Cohen M.H., Ogle P.M., Tran H.D., Vermeulen R.C., Miller J.S., Goodrich R.W., Martel A.R., 1995, ApJ, 448, L77
Cohen M.H., Vermeulen R.C., Ogle P.M., Tran H.D., Goodrich R.W., 1997, ApJ, 484, 193
Cohen M.H., Ogle P.M., Tran H.D., Goodrich R.W., Miller J.S., 1999, AJ, 118, 1963
Dey A., Spinrad H., 1996, ApJ, 459, 133
Dey A., van Breugel W., Vacca W.D., Antonucci R., 1997, ApJ, 490, 698
Dickson R., Tadhunter C., Shaw M., Clark N., Morganti R., 1995, MNRAS, 273, L29
di Serego Alighieri S., Fosbury R.A.E., Tadhunter C.N., Quinn P.J., 1989, Nat, 341, 307
di Serego Alighieri S., Cimatti A., Fosbury R.A.E., 1993, ApJ, 404, 584
di Serego Alighieri S., Cimatti A., Fosbury R.A.E., 1994, ApJ, 431, 123
di Serego Alighieri S., Cimatti A., Fosbury R.A.E., Perez-Fournon I., 1996, MNRAS, 279, L57
Dopita M.A., Sutherland R.S., 1996, ApJS, 102, 161
Dunlop J.S., Peacock J.A., Savage A., Lilly S.J., Heasley J.N., Simon A.J.B., 1989, MNRAS, 238, 1171
Fabian A.C., 1989, MNRAS, 238, 41P
Kapahi V.K., Athreya R.M., van Breugel W., McCarthy P.J., Subrahmanya C.R., 1998, ApJS, 118, 275
Kishimoto M., Antonucci R., Cimatti A., Hurt T., Dey A., van Breugel W., Spinrad H., 2001, ApJ, 547, 667
McCarthy P.J., 1993, ARA&A, 31, 639
McCarthy P.J., van Breugel W., Spinrad H., Djorgovski S., 1987, ApJ, 321, L29
McCarthy P.J., van Breugel W., Kapahi V.K., 1991, ApJ, 371, 478
McLure R.J., Dunlop J.S., 2000, MNRAS, 317, 249
Maddox S.J., Efstathiou G., Sutherland W.J., Loveday J., 1990, MNRAS, 243, 692
Manzini A., di Serego Alighieri S., 1996, A&A, 311, 79
Mathis J.S., Rumpl W., Nordsieck K.H., 1977, ApJ, 217, 425
Mellema G., Kurk J.D., Röttgering H.J.A., 2002, A&A, 395, L13
Osterbrock D.E., 1989, Astrophysics of Gaseous Nebulae and Active Galactic Nuclei. Univ. Science Books, Mill Valley, CA
Rees M.J., 1989, MNRAS, 239, 1P
Röttgering H.J.A., Lacy M., Miley G.K., Chambers K.C., Saunders R., 1994, A&AS, 108, 79
Schmidt G.D., Elston R., Lupie O.L., 1992, AJ, 104, 1563
Seaton M.J., 1979, MNRAS, 187, 73P
Serkowski K., Mathewson D.L., Ford V.L., 1975, ApJ, 196, 261

Shaw M., Tadhunter C., Dickson R., Morganti R., 1995, MNRAS, 275, 703
Solórzano-Iñarrea C., Tadhunter C.N., 2003, MNRAS, 340, 705
Solórzano-Iñarrea C., Tadhunter C.N., Axon D.J., 2001, MNRAS, 323, 965
Stockman H.S., Angel J.R.P., Miley G.K., 1979, ApJ, 227, L55
Tadhunter C.N., Fosbury R.A.E., di Serego Alighieri S., 1988, in Maraschi L., Maccacaro T., Ulrich M.H., eds, Proc. Como Conf., BL Lac Objects. Springer-Verlag, Berlin, p. 79
Tadhunter C.N., 1986, PhD thesis, Univ. Sussex
Tadhunter C.N., Scarrott S.M., Draper P., Rolph C., 1992, MNRAS, 256, 53P
Tadhunter C.N., Dickson R., Morganti R., Robinson T.G., Wills K., Villar-Martín M., Hughes M., 2002, MNRAS, 330, 977
Telfer R.C., Zheng W., Kriss G.A., Davidsen A.F., 2002, ApJ, 565, 773
Turnshek D.A., Bohlin R.C., Williamson R.L., Lupie O.L., Koornneef J., Morgan D.H., 1990, AJ, 99, 1243
Vernet J., 2001, PhD thesis, Université Paris VII
Vernet J., Fosbury R.A.E., Villar-Martín M., Cohen M.H., Cimatti A., di Serego Alighieri S., Goodrich R.W., 2001, A&A, 366, 7
Zubko V.G., Laor A., 2000, ApJS, 128, 245

This paper has been typeset from a TEX/LATEX file prepared by the author.